

1 Magma degassing in the effusive-explosive subglacial rhyolitic  
2 eruption of Dalakvísl, Torfajökull, Iceland: insights into  
3 quenching pressures, palaeo-ice thickness, and edifice erosion

4

5 Jacqueline Owen<sup>a\*</sup>, Hugh Tuffen<sup>a</sup>, Dave McGarvie<sup>a</sup>

6 <sup>a</sup>Lancaster Environment Centre, Lancaster University, Lancaster, LA1 4YQ. UK

7 \*j.owen2@lancaster.ac.uk

8

9 **1 Abstract**

10 Dissolved volatile contents preserved in the matrix glass of subglacially erupted rocks  
11 offer important insights into quenching pressures. With careful interpretation, these data  
12 may yield information on eruption conditions. In this paper we present detailed edifice and  
13 glacier reconstructions for explosive and effusive subglacial rhyolitic deposits at Dalakvísl,  
14 Torfajökull, Iceland. When grouped by lithofacies, Dalakvísl glasses display trends of  
15 decreasing H<sub>2</sub>O with elevation, consistent with a subglacial setting. A number of solubility  
16 pressure curves (SPCs) have been used to model these quenching pressure-elevation trends  
17 in order to reconstruct the loading conditions. Effusively erupted glasses (e.g. lava lobes) have  
18 higher dissolved water contents than the more explosively produced material (e.g. obsidian  
19 sheets), indicating a systematic difference in subglacial pressure and/or degassing behaviour.  
20 Best model fits to data are achieved when loading is by a combination of erupted deposits  
21 (with a flat-topped morphology) and ice/meltwater. Our best estimate for the original edifice  
22 summit elevation is ~810 m a.s.l., similar to its current elevation; however, as the edifice is  
23 now more conical this indicates significant post-eruptive erosion around the margins of the  
24 edifice. We propose that during the initial stages of the eruption, meltwater could not escape,

25 thus maintaining high subglacial pressure under which effusive lava bodies were produced  
26 intrusively. Our best estimate is that the original palaeo-ice surface was ~1,020 m a.s.l.,  
27 suggesting a syn-eruptive glacier thickness of ~350 m, assuming a similar base level to today  
28 (~670 m a.s.l.). A sudden release of meltwater then led to a pressure drop, driving a transition  
29 to more explosive activity with an ice surface over the vent closer to 880 m a.s.l. This study  
30 demonstrates the uses of dissolved volatile contents in reconstructing past environments and  
31 shows how eruption dynamics can be tracked over the timeline of a pre-historic eruption,  
32 offering valuable insight into the complex coupling between pressure and the mechanisms of  
33 subglacial eruptions.

34

35 **Keywords** subglacial · rhyolite · explosive-effusive transition · water solubility · infra-  
36 red spectroscopy · Iceland · volcano-ice interactions

37

## 38 **2 Introduction**

### 39 **2.1 Research Goals**

40 Although eyewitness accounts and monitoring of recent eruptions are perhaps the  
41 greatest source of accurate data, capturing such accounts can be difficult to achieve,  
42 especially for subglacial settings. Firstly, subglacial volcanoes can be extremely explosive due  
43 to violent fuel-coolant interactions and are therefore dangerous to monitor (Duncan et al.,  
44 1986; Mastin et al., 2004; Stevenson et al., 2011). Secondly, some, if not all, of the deposits  
45 will be obscured by the glacier (Tómasson, 1996; Owen, 2016). Thirdly, a subglacial rhyolite  
46 eruption has never been observed (Guðmundsson, 2003; Tuffen et al., 2008). Therefore, in

47 order to understand subglacial rhyolitic volcanism, we need to turn to past eruptions (Owen,  
48 2016).

49 This paper focuses on the subglacial rhyolite eruption at Dalakvísl in southern Iceland,  
50 which was part of one of Iceland's largest known subglacial rhyolitic eruptions, from  
51 Torfajökull at 70 ka (McGarvie et al., 2006; Tuffen et al., 2008). The Dalakvísl deposits record  
52 both explosive and effusive activity (Tuffen et al., 2008) and may provide insight into  
53 mechanisms of subglacial rhyolitic volcanism. Consequently it has been well studied: Tuffen  
54 et al. (2008) documented the erupted lithofacies; Owen et al. (2013a) measured pre-eruptive  
55 volatiles and reconstructed degassing paths for Dalakvísl and four other subglacial Torfajökull  
56 edifices, deducing that magmatic degassing was the main influence on eruptive style; and  
57 Owen et al. (2013b) incorporated dissolved volatile concentrations and vesicle textures to  
58 further investigate the transition in eruptive style at Dalakvísl, deducing that it coincided with  
59 and was likely caused by a sudden pressure drop, most likely triggered by a jökulhlaup.

60 This paper will use dissolved volatile concentrations from Owen et al. (2013b) to  
61 calculate quenching pressures in order to reconstruct the palaeo-ice thickness, eruptive  
62 setting (i.e. whether outcrops formed intrusively or extrusively), original edifice morphology  
63 and erosion history. This will aid future interpretations of subglacial rhyolitic lithofacies,  
64 improve understanding of the way in which subglacial rhyolitic edifices erode, shed light on  
65 past climates, and explore links between eruptive style and ice thickness.

## 66 ***2.2 Volatile-based palaeo-ice reconstructions***

67 The majority of volcano based palaeo-ice reconstructions have relied on the elevation  
68 of subglacial-to-subaerial lithofacies transitions at tuyas; edifices where erupting material  
69 broke through the surface of ice sheets (Mathews, 1947; Jones, 1966; McGarvie et al., 2006;

70 Edwards et al., 2011; Owen, 2016). However, due to increased understanding of water  
71 solubility-pressure relationships (Newman et al., 1988; Dixon and Stolper, 1995; Dixon, 1997;  
72 Newman and Lowenstern, 2002) a new technique is being refined (Tuffen et al., 2010; Owen,  
73 2016) whereby the dissolved water content of glassy eruptive material can be used to  
74 reconstruct quenching pressures (e.g. Saubin et al., 2016) and therefore estimate palaeo-ice  
75 thicknesses (Dixon et al., 2002; Höskuldsson et al., 2006; Schopka et al., 2006; Edwards et al.,  
76 2009; Owen et al., 2012).

77         The technique utilises the pressure dependence of water solubility in silicate melts.  
78 Rise and decompression of volatile-saturated magma results in volatile exsolution, which  
79 depletes the residual melt in dissolved volatiles (Gonnermann and Manga, 2007). Assuming  
80 equilibrium degassing, the dissolved volatile content in volcanic glasses should record the  
81 quenching pressure (Tuffen et al., 2010). In subglacial settings, this can be converted into  
82 palaeo-ice thicknesses so long as subglacial cavity pressure equals glaciostatic pressure from  
83 the overlying ice burden (Tuffen et al., 2010). However, non-glaciostatic pressure may  
84 develop, depending on the local volume flux (input of erupted material vs volume of ice  
85 melted) and extent of meltwater drainage (Guðmundsson et al., 2004; Tuffen et al., 2010).  
86 Furthermore, quenching pressure may reflect loading by rock, as well as ice or meltwater,  
87 giving a greater increase in pressure with elevation due to the higher density of the loading  
88 medium (Tuffen and Castro, 2009).

89         Although factors such as volatile undersaturated melt and non-glaciostatic pressure  
90 may hinder reconstructions of palaeo-ice thickness, such palaeo-pressure reconstructions  
91 may constrain aspects of subglacial hydrology (Höskuldsson et al., 2006; Schopka et al., 2006;  
92 Owen et al., 2013b), edifice erosion (Stevenson et al., 2009; Tuffen and Castro, 2009; Owen

93 et al., 2012) and pre-eruptive volatile content (Dixon et al., 2002; McGarvie et al., 2007; Owen  
94 et al., 2012).

95 Another major advantage of this technique is that it is not limited to tuyas but is also  
96 applicable to non-emergent, wholly subglacial edifices.

97

### 98 **2.3 Geological background**

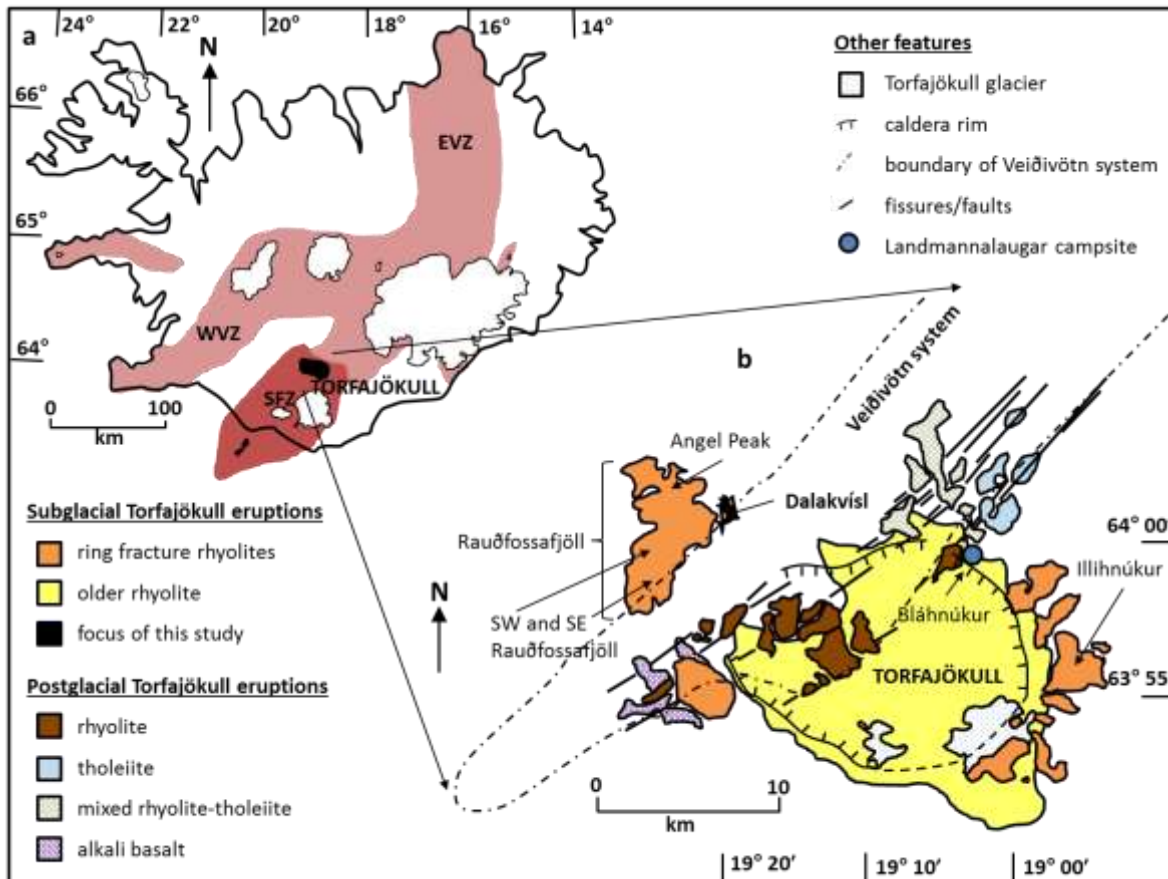
99 Iceland hosts >30 active volcanic systems, which typically consist of a central volcano  
100 and associated fissure swarms. Of these, at least 23 have produced subglacial rhyolite in the  
101 last 0.8 Ma (McGarvie, 2009). Rhyolitic volcanism is mostly limited to central volcanoes  
102 (Sigurdsson, 1977; Sæmundsson, 1979; Imsland, 1983), as rhyolite petrogenesis involves both  
103 fractional crystallisation and partial re-melting of the crust (Gunnarsson et al., 1998; Martin  
104 and Sigmarsson, 2007; Zellmer et al., 2008; Martin and Sigmarsson, 2010). As most Icelandic  
105 central volcanoes have erupted ~10% rhyolite (Imsland, 1983) and a third of 20<sup>th</sup> century  
106 Icelandic eruptions were subglacial (Guðmundsson, 2005) subglacial rhyolitic eruptions  
107 constitute an important part of past and future volcanism in Iceland.

108 Torfajökull central volcano is located in southern Iceland (**Fig. 1a**) where the Eastern  
109 Volcanic Zone (EVZ) propagates southwards into the Southern Flank Zone (SFZ). With 80%  
110 rhyolite (Gunnarsson et al., 1998) Torfajökull is Iceland's largest producer of silicic magma,  
111 attributed to enhanced melting of older crust (Sigurdsson, 1977; Martin and Sigmarsson,  
112 2007). Torfajökull demonstrates a great diversity in subglacial rhyolitic edifices (Sæmundsson,  
113 1972; McGarvie, 1984; McGarvie et al., 2006; McGarvie, 2009), ranging from small volume  
114 effusive edifices such as Bláhnúkur (**Fig. 1b**), consisting of lava lobes and quench hyaloclastite  
115 (Furnes et al., 1980; Tuffen et al., 2001; McGarvie, 2009), to steep-sided tuyas such as SE

116 Rauðfossafjöll (**Fig. 1b**), which consist of fine-grained pyroclastic material capped by subaerial  
117 lava flows (Tuffen et al., 2002; McGarvie, 2009).

118 The ~70 ka rhyolitic eruption from Torfajökull, with >16 km<sup>3</sup> total preserved erupted  
119 volume (McGarvie et al., 2006), is one of the largest known silicic eruptions in Iceland and the  
120 largest known subglacial rhyolite event. Edifices constructed during this eruption form a ring  
121 around Torfajökull (McGarvie et al., 2006), hereafter known as the ring fracture rhyolites (**Fig.**  
122 **1b**). All ring fracture edifices may derive from a single eruptive event (MacDonald et al., 1990;  
123 McGarvie et al., 1990) for which two samples provide Ar-Ar dates of 67.2 ±9.1 ka and 71.5  
124 ±7.4 ka (McGarvie et al., 2006). However, Brendryen et al. (2010) have also identified  
125 Torfajökull rhyolites in a North Atlantic marine core. Similar compositions and ages  
126 (Brendryen et al., 2010) suggest these layers represent ring fracture rhyolites. These North  
127 Atlantic ash layers indicate that an additional significant volume of ash was widely distributed  
128 out to sea during this event, requiring higher estimates of the total erupted volume.  
129 Furthermore, interspersing of the rhyolitic layers with basaltic horizons over an 800 year  
130 period (Brendryen et al., 2010), challenges the model for a single eruptive event (MacDonald  
131 et al., 1990; McGarvie et al., 1990), instead favouring a scenario where the ring fracture  
132 rhyolites erupted in pulses, over an 800 year period or more.

133



134

135 **Figure 1:** Maps modified from Owen et al. (2012): **(a)** Simplified geological map of Iceland, showing  
 136 the location of Torfajökull, based on Larsen (1984) and Gunnarsson et al. (1998). WVZ: West Volcanic  
 137 Zone, EVZ: East Volcanic Zone, SFZ: Southern Flank Zone. **(b)** Simplified geological map of Torfajökull,  
 138 showing the location of Dalakvísl, based on Blake (1984), McGarvie (1984), Gunnarsson et al. (1998)  
 139 and McGarvie et al. (2006).

140 Based on its geochemistry and position, Dalakvísl is one of the edifices attributed to  
 141 the 70 ka event (Tuffen et al., 2008). It occurs at the northern fringe of the Rauðfossafjöll  
 142 rhyolite massif in western Torfajökull (**Fig. 1b**), where there are four large tuyas, each  
 143 exceeding 1 km<sup>3</sup> in volume and with 1,174-1,235 m summit elevations (Tuffen et al., 2002).  
 144 By contrast, the summit elevation of Dalakvísl is 810 m and the deposit volume <0.2 km<sup>3</sup>

145 (Tuffen et al., 2008). Nonetheless, fragmental lithofacies at Dalakvísl are similar to those at  
146 the Rauðfossafjöll tuyas, including fine-grained pumiceous pyroclastic deposits typical of  
147 explosive activity (Stevenson et al., 2011). Crudely bedded fragmental deposits at Dalakvísl  
148 (**Figs. 2di,ii; 'cba' in Figure 3**) suggest an aqueous subglacial setting and provide the first  
149 documented evidence for localised meltwater ponding during a subglacial rhyolitic eruption  
150 (Tuffen et al., 2008). However, Dalakvísl lithofacies also include lava lobe-bearing hyaloclastite  
151 (**Figs. 2ai,ii; 'cj' in Figure 3**) (Tuffen et al., 2008), which resembles the products of an effusive  
152 subglacial rhyolite eruption at Bláhnúkur, Torfajökull (Tuffen et al., 2001). The hyaloclastite  
153 consists of perlitised obsidian breccia and blocky, low vesicularity ash shards. Lava lobes are  
154 crudely conical, generally 5-10 m wide and 3-5 m thick, with a microcrystalline interior and  
155 dense obsidian carapace, and their vesicularity is generally < 5%. Columnar-jointed upper  
156 surfaces are thought to show ice contact, indicating that lava lobes formed within subglacial  
157 cavities at the glacier base (Tuffen et al., 2008).

158         The variety of explosive and effusive lithofacies at Dalakvísl therefore indicates that  
159 the eruption underwent a change in eruptive behaviour. A pyroclastic deposit containing  
160 obsidian sheets is of particular interest regarding the transition in eruptive style (**Figs. 2bi-iii;**  
161 **'os' in Figure 3**). Sheets are 0.5-1 m thick and 1-20 m long lava bodies that occupy 10 volume  
162 % of a pumiceous pyroclastic breccia. They consist of three zones (**Fig. 2biii**): an inner core of  
163 relatively dense obsidian (zone 1) and an outer zone of pumice (zone 3), with a transitional  
164 zone separating the two (zone 2). The sheets have a jigsaw fit with the surrounding breccia,  
165 which is thought to be composed of earlier disintegrated sheets. As lava body size, vesicularity  
166 and grain size distribution for this deposit (Owen et al., 2013b) all fall between the lava lobe  
167 deposits (effusive endmember) and the crudely bedded ash (explosive endmember), the

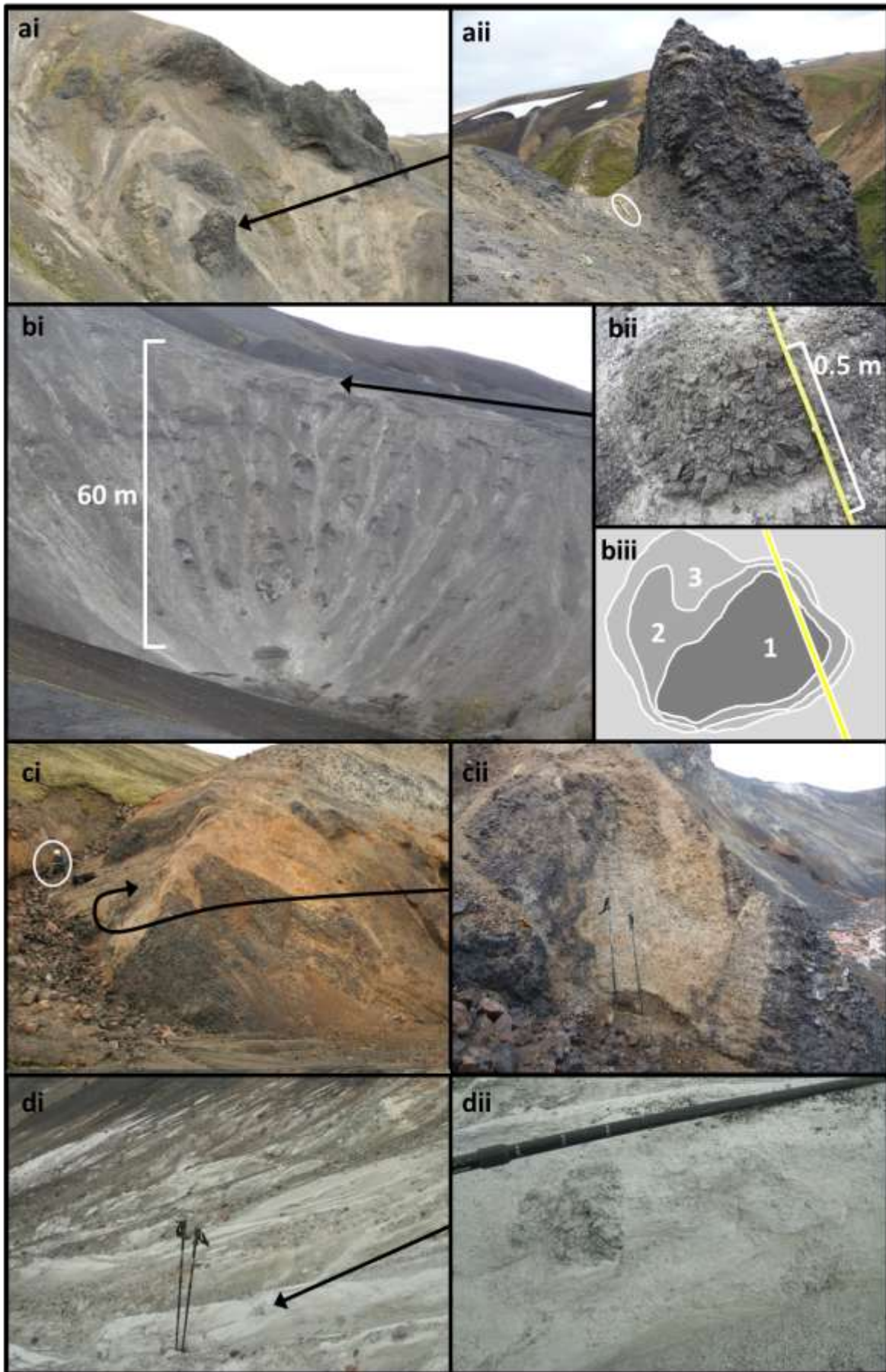


168 obsidian sheet deposit is thought to encapsulate transitional behaviour at Dalakvísl (Tuffen et  
169 al., 2008).

170 Tuffen et al. (2008) used obsidian sheet vesicle textures (**Fig. 2bii**) to propose  
171 formation when a vesiculating, incompletely fragmented magma intruded within overlying  
172 pyroclastic debris, triggering partial foam collapse that generated the sheets and drove a  
173 transition from explosive to effusive activity. This theory is contested by Stevenson et al.  
174 (2011) and Owen et al. (2013b), who favour a model of *in-situ* localised vesiculation.

175 Other lithofacies at Dalakvísl (**Fig. 3**) include perlitised lava, poorly exposed obsidian  
176 mounds (referred to as 'miscellaneous' or 'misc.' in figures) and remobilised deposits of  
177 obsidian sheets and lava lobes (referred to as 'juxtaposed obsidian' in figures) (**Figs. 2ci,ii**).

178



180

181 **Figure 2:** Dalakvísl lithofacies (see **Figure 3** for sample locations). **(ai)** Dark lava lobes (5-40 m long)  
182 protrude from massive obsidian and pumice breccia (looking NE towards D1-D4). **(aii)** A single  
183 columnar-jointed lava lobe (locality D1), with a geological hammer for scale (outlined with white  
184 circle). **(bi)** Dark obsidian sheets (1-10 m long) surrounded by pale ash-pumice breccia (looking N  
185 towards D11-D16). **(bii)** A small obsidian sheet with a metre rule for scale (locality D16). **(biii)** A  
186 schematic representation of **Figure 2bii**. Numbers indicate textural zones: 1 - dark grey vesicle-poor  
187 obsidian; 2- medium grey, moderately vesicular obsidian; 3 - pale grey pumice. **(ci)** A deposit of  
188 deformed sheet and lobe portions juxtaposed with variably vesicular obsidian and pumiceous breccia  
189 and cut through by faults (looking N towards D5) with person for scale (outlined with white circle).  
190 **(cii)** A more detailed view of the deposit in part **ci**, walking poles are 1.2 m long. **(di)** A deposit of  
191 crudely bedded ash (cba), looking W towards D7. **(dii)** A pumiceous clast within the cba deposit.

#### 192 **2.4 Previous constraints on the ice thickness at Dalakvísl**

193 The syn-eruptive ice thickness at Dalakvísl, was estimated at 300-400 m (Tuffen et al.,  
194 2008) based on water concentrations in a single obsidian sheet. However, it is now clear that  
195 complex degassing patterns in even small-volume subglacial eruptions require multiple  
196 sampling for robust ice thickness measurements (Owen et al., 2012; Owen, 2016).

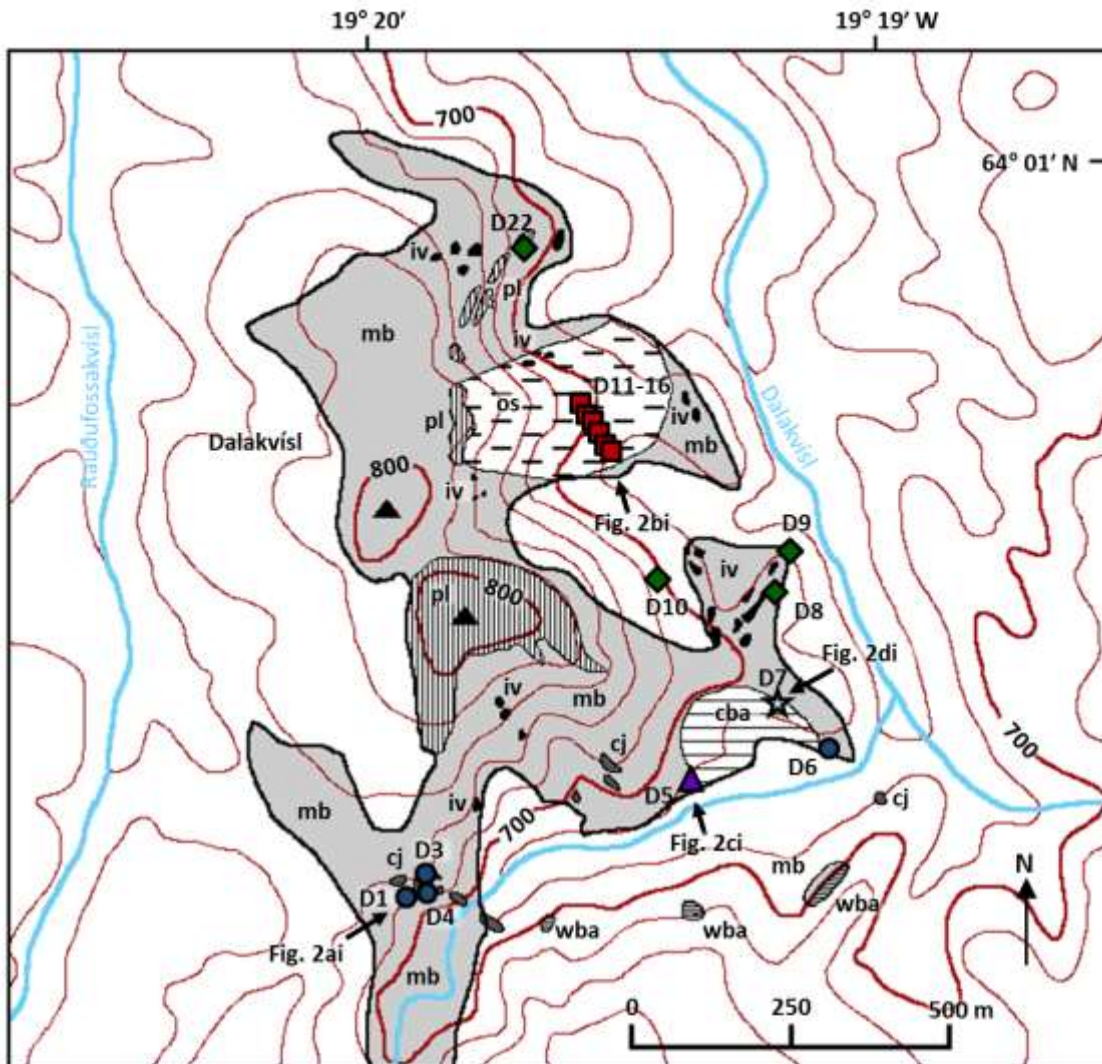
197 Thus, further work is needed to 1) better constrain the ice thickness at Dalakvísl 2)  
198 investigate different loading mediums to better understand where there has been intrusive  
199 and extrusive formation; and 3) understand subglacial pressure conditions in an eruption that  
200 straddled the explosive-effusive transition.

## 201 **3 Methods**

### 202 ***3.1 Sample collection***

203           Twenty-nine obsidian samples were collected from 16 localities (**Fig. 3**) and are the  
204 same as those used in the Owen et al. (2013b) study. The samples encompass a wide range  
205 of elevations, lithofacies and positions (**Table 1**). All three textural zones within obsidian  
206 sheets were sampled (**Fig. 2biii**). All collected samples are glassy; those showing evidence for  
207 perlitisation or post-quenching movement were avoided. In addition, one ash sample (D7a)  
208 was collected for geochemical analysis.

209



**Map symbols**

- 800 elevation (m)
- summit
- stream

**Dalakvísl formation**

- extent of Dalakvísl formation
- massive breccia with obsidian sheets
- irregular vesicular peperitic lavas
- massive obsidian and pumice breccia
- columnar jointed lava lobes
- well-bedded ash
- perlitised lava
- crudely bedded ash

**Sampling locations**

- lava lobes
- miscellaneous
- juxtaposed obsidian
- obsidian sheets
- fine grained ash
- location and direction of photographs in Figure 2

211 **Figure 3:** A geological map of Dalakvísl, modified from Tuffen et al. (2008), showing the sampling  
 212 locations. Coloured symbols represent lithofacies (**Table 1**) and are used throughout the paper as per  
 213 the legend.

214

215 **Table 1:** A brief summary of sample descriptions, sampling locations and the analytical work done on  
 216 each.

Sample name	GPS coordinates	Elevation (m) <sup>a</sup>	Reference facies unit <sup>b</sup>	Sample description <sup>d</sup>	Locality description	Inferred eruptive behaviour	FTIR	XRF	Figs. <sup>g</sup>
D1	N 64 00 22.6, W019 19 51.5	725	cj	ob	lava lobe	effusive	yes	yes	2ai,ii
D3	N 64 00 23.8, W019 19 53.2	760	cj	ob	lava lobe	effusive	yes	/	2ai,ii
D4		730	cj	ob	lava lobe	effusive	yes	/	2ai,ii
D5a	N 64 00 28.6, W019 19 18.3	680	iv/cj	ob	juxtaposed ob	? <sup>f</sup>	yes	/	2ci,ii
D5b	N 64 00 28.6, W019 19 18.3	680	iv/cj	pum	juxtaposed ob	? <sup>f</sup>	yes	/	2ci,ii
D6	N 64 00 30.0, W019 19 04.0	695	cj	ob	lava lobe	effusive	yes	/	/
D7a	N 64 00 32.2, W019 19 10.7	707	cba	ash	fine ash	explosive	/	yes	2di,ii
D7b	N 64 00 32.2, W019 19 10.7	707	cba	pum clast	fine ash	explosive	yes	/	2di,ii
D8	N 64 00 38.0, W019 19 10.7	701	iv	ob	misc. <sup>e</sup>	? <sup>f</sup>	yes	/	/
D9	N 64 00 40.0, W019 19 09.0	674	mb	ob	misc. <sup>e</sup>	? <sup>f</sup>	yes	/	/
D10	N 64 00 38.5, W019 19 24.6	725	pl <sup>c</sup>	ob	misc. <sup>e</sup>	? <sup>f</sup>	yes	/	/
D11a	N 64 00 45.0, W019 19 29.2	668	os	ob	sheet	transition	yes	/	2bi-iii
D11b	N 64 00 45.0, W019 19 29.2	668	os	tran	sheet	transition	yes	/	2bi-iii
D11c	N 64 00 45.0, W019 19 29.2	668	os	pum	sheet	transition	yes	/	2bi-iii
D12a	N 64 00 45.3, W019 19 29.8	678	os	ob	sheet	transition	yes	/	2bi-iii
D12b	N 64 00 45.3, W019 19 29.8	678	os	tran	sheet	transition	yes	/	2bi-iii
D12c	N 64 00 45.3, W019 19 29.8	678	os	pum	sheet	transition	yes	/	2bi-iii
D13a	N 64 00 45.3, W019 19 31.0	692	os	ob	sheet	transition	yes	yes	2bi-iii
D13b	N 64 00 45.3, W019 19 31.0	692	os	tran	sheet	transition	yes	/	2bi-iii
D13c	N 64 00 45.3, W019 19 31.0	692	os	pum	sheet	transition	yes	/	2bi-iii
D14a	N 64 00 46.3, W019 19 31.9	701	os	ob	sheet	transition	yes	/	2bi-iii
D14b	N 64 00 46.3, W019 19 31.9	701	os	tran	sheet	transition	yes	/	2bi-iii
D14c	N 64 00 46.3, W019 19 31.9	701	os	pum	sheet	transition	yes	/	2bi-iii
D15a	N 64 00 47.0, W019 19 32.0	711	os	ob	sheet	transition	yes	/	2bi-iii
D15b	N 64 00 47.0, W019 19 32.0	711	os	tran	sheet	transition	yes	/	2bi-iii
D15c	N 64 00 47.0, W019 19 32.0	711	os	pum	sheet	transition	yes	/	2bi-iii
D16a	N 64 00 47.4, W019 19 33.7	722	os	ob	sheet	transition	yes	/	2bi-iii
D16b	N 64 00 47.4, W019 19 33.7	722	os	tran	sheet	transition	yes	/	2bi-iii
D16c	N 64 00 38.0, W019 19 10.7	722	os	pum	sheet	transition	yes	/	2bi-iii
D22	N 64 00 55.8, W019 19 40.1	720	pl <sup>c</sup>	ob	misc. <sup>e</sup>	? <sup>f</sup>	yes	yes	/

217

218 a elevations determined by handheld GPS. The uncertainty for these measurements is  $\pm 10$  m

- 219 b the unit to which the sample belongs according to the geological map of Tuffen et al. (2008), where a full  
 220 description and interpretation of each lithofacies can be found. See **Figure 3** for a modified version, with brief facies  
 221 descriptions where cj = columnar jointed lava lobes, iv = irregular vesicular peperitic lavas, cba = crudely bedded  
 222 ash, mb = massive obsidian and pumice breccia, pl = perlitised lava and os = massive breccia with obsidian sheets.  
 223 c a non-perlitised sample from the 'perlitised lava' facies described in Tuffen et al. (2008)  
 224 d sample description where ob = low vesicularity obsidian, pum = highly vesicular pumice, tran = transitional between  
 225 dense obsidian and vesicular pumice  
 226 e 'misc.' refers to poorly exposed mound of dense obsidian  
 227 f '?' refers to a sample from which the eruptive behaviour at that locality cannot be inferred  
 228 g reference to sample photographs where a more detailed locality description can be found

### 229 **3.2 Water concentration measurements using infra-red spectroscopy**

230 Dissolved water contents were measured using Fourier Transform Infrared  
 231 Spectroscopy (FTIR). Samples were doubly hand-polished to create wafers with thicknesses  
 232 measured using a Mitutoyo digital displacement gauge accurate to  $\pm 3 \mu\text{m}$ . FTIR  
 233 measurements were carried out on the same spot as measured by the displacement gauge.  
 234 FTIR analysis was done at the Open University, Milton Keynes, with a Thermo Nicolet  
 235 Continuum Analytical microscope, a KBr beamsplitter, a liquid nitrogen cooled MCT-A  
 236 detector and a  $\text{N}_2$  purged tank to reduce background contamination. For every sample a  
 237 background (of 256 scans) was performed, followed by  $\geq 5$  analyses, with 256 scans collected  
 238 between  $650$  and  $5000 \text{ cm}^{-1}$ , a  $100 \mu\text{m}$  square aperture and  $4 \text{ cm}^{-1}$  resolution. A 15 point linear  
 239 baseline correction was applied to the resulting spectra (**Fig. 4**). Peak heights were converted  
 240 into water contents ( $C_{\text{H}_2\text{O}}$ ) using the Beer-Lambert Law:

241

$$242 \quad C_i = \frac{M_i \text{Abs}}{d \rho \epsilon} \quad \text{Equation 1}$$

243 where  $i$  refers to the volatile species of interest,  $M_i$  is molecular weight,  $\text{Abs}$  is  
 244 absorbance (measured peak height),  $d$  is sample thickness (in cm),  $\rho$  is sample density (in  $\text{g l}^{-1}$ )  
 245 and  $\epsilon$  is the absorption coefficient (in  $\text{l mol}^{-1} \text{ cm}^{-1}$ ).

246 The  $3,550 \text{ cm}^{-1}$  and  $1,630 \text{ cm}^{-1}$  peaks were used to measure total water ( $\text{H}_2\text{O}_t$ ) and  
 247 molecular water ( $\text{H}_2\text{O}_m$ ) (**Fig. 4**), using absorption coefficients of  $80 \text{ l mol}^{-1} \text{ cm}^{-1}$  (Leschik et al.,

248 2004) and  $55 \text{ l mol}^{-1} \text{ cm}^{-1}$  (Newman et al., 1986) respectively. Spectra were rejected in which  
249 the strong  $\text{H}_2\text{O}_t$  absorption band was saturated; for a mean sample value to be considered  
250 reliable, we required a minimum of three of the spectra to be usable. The density of Dalakvísl  
251 obsidian was taken to be  $2.41 \pm 0.01 \text{ g cm}^{-3}$  based on density measurements of non-vesicular  
252 samples using the Archimedes method. The molecular weight of water is  $18.02 \text{ g mol}^{-1}$ .

253 None of the samples produced a measureable  $4,520 \text{ cm}^{-1}$  hydroxyl ( $\text{OH}^-$ ) peak, due to  
254 the combination of low wafer thickness ( $<200 \mu\text{m}$ ) and water content of  $<1 \text{ wt.}\%$  (Okumura  
255 et al., 2003; Leschik et al., 2004). Similarly, the  $2,350 \text{ cm}^{-1}$  peak was always indiscernible,  
256 therefore  $\text{CO}_2$  concentrations are deemed to fall beneath the detection limit of 30 ppm (**Fig.**  
257 **4**).

258 As demonstrated in Owen et al. (2012), error values are highly influenced by sample  
259 thickness. For typical Dalakvísl samples,  $\text{H}_2\text{O}_t$  error is  $\pm 7.0\%$  and comparative error is  
260 considerably smaller ( $\pm 2.4\%$ ) as the same methodology and absorption coefficients were used  
261 for all samples (Owen, 2013). This is within the 10 %  $\text{H}_2\text{O}_t$  error value commonly used in FTIR  
262 studies (e.g. Dixon et al., 1995; Dixon and Clague, 2001; Dixon et al., 2002; Nichols et al., 2002;  
263 Nichols and Wysoczanski, 2007; Tuffen and Castro, 2009; Tuffen et al., 2010). Larger  $\text{H}_2\text{O}_m$   
264 error, up to  $\pm 20\%$  (Dixon and Clague, 2001; Dixon et al., 2002), is partially due to a hidden  
265 alumina-silicate peak at  $1600 \text{ cm}^{-1}$  (Newman et al., 1986). However, in this study,  $\text{H}_2\text{O}_m$  is only  
266 used in a relative fashion, to identify hydrated samples.

267

### 268 **3.3 Geochemistry**

269 A small but representative sub-set of four samples was analysed for geochemistry.  
270 Bulk rock major and trace element concentrations were measured using the X-Ray



271 Fluorescence (XRF) facility at the University of Edinburgh with a Panalytical PW2404  
272 wavelength-dispersive sequential X-ray spectrometer. Errors were determined by repeatedly  
273 analysing standards of known composition (Owen, 2013).

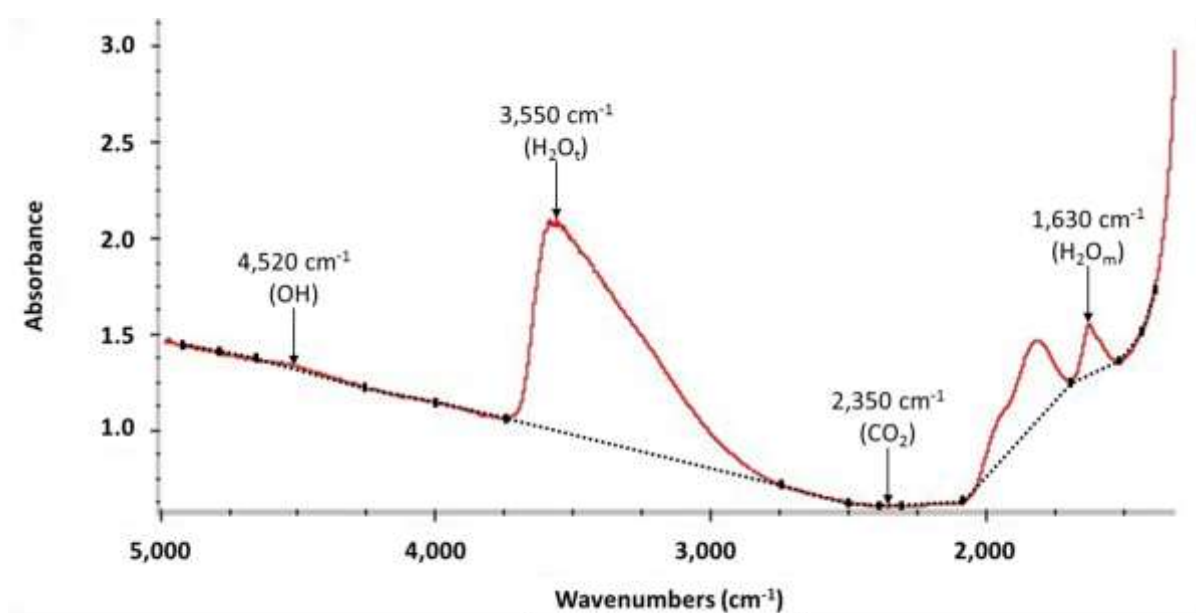
## 274 4 Results

### 275 4.1 Dissolved water content (FTIR)

276 Of the 29 samples analysed for water contents using FTIR, nine failed to produce any useable  
277 results due to peak saturation, reflecting difficulty in preparing sufficiently thin wafers of  
278 vesicular samples. Thus, a data-set of 20 samples was produced (Table 2).

279

280



281

282 **Figure 4:** A typical FTIR spectrum (sample D22). The small black rectangles and dashed line mark the  
283 position of the 15 point baseline correction before it has been applied. Peaks of interest are indicated.

284 H<sub>2</sub>O<sub>t</sub> and H<sub>2</sub>O<sub>m</sub> peaks are seen in every spectrum but OH<sup>-</sup> and CO<sub>2</sub> peaks are always too small to  
 285 accurately measure.

286

287 **Table 2:** Averaged FTIR data. Errors for H<sub>2</sub>O<sub>t</sub> and H<sub>2</sub>O<sub>m</sub> are ± 7-10% and 20% respectively, although  
 288 comparative errors will be considerably smaller. Modified from Owen et al. (2013b).

Sample name	Sample thickness (µm) <sup>a</sup>	FTIR points per sample <sup>b</sup>	Total water (H <sub>2</sub> O <sub>t</sub> )			Molecular water (H <sub>2</sub> O <sub>m</sub> )		
			3,550 peak height <sup>c</sup>	Mean H <sub>2</sub> O <sub>t</sub> (wt.%) <sup>d</sup>	St. dev. H <sub>2</sub> O <sub>t</sub> (wt.%) <sup>e</sup>	1,630 peak height <sup>c</sup>	Mean H <sub>2</sub> O <sub>m</sub> (wt.%) <sup>d</sup>	St. dev. H <sub>2</sub> O <sub>m</sub> (wt.%) <sup>e</sup>
D1	312	5	2.141	0.64	0.03	0.616	0.27	0.01
D3	95	5	0.594	0.58	0.02	0.153	0.22	0.03
D4	89	4	0.593	0.62	0.02	0.279	0.42	0.02
D5a	109	5	0.887	0.76	0.03	0.219	0.27	0.02
D5b	141	31	0.498	0.33	0.08	0.108	0.10	0.01
D6	47	5	0.349	0.69	0.03	0.126	0.36	0.03
D8	294	5	1.702	0.54	0.02	0.450	0.21	0.00
D9	58	5	0.530	0.85	0.01	0.142	0.33	0.02
D10	77	5	0.411	0.50	0.04	0.109	0.19	0.01
D11c	214	3	1.601	0.70	0.01	0.918	0.58	0.03
D12a	186/259	10	1.604	0.67	0.02	0.295	0.18	0.01
D12b	304	5	1.914	0.59	0.01	0.343	0.15	0.01
D13a	348	5	2.375	0.64	0.01	0.452	0.18	0.00
D13b	330	4	2.038	0.58	0.07	0.355	0.15	0.01
D14b	333	5	1.995	0.56	0.03	0.322	0.13	0.01
D14c	282	1	1.882	0.62	/	0.906	0.44	/
D15a	345	5	2.101	0.57	0.01	0.415	0.16	0.01
D16a	245	5	1.337	0.51	0.01	0.224	0.12	0.00
D16b	308	5	1.600	0.48	0.00	0.261	0.12	0.00
D22	204	5	1.170	0.53	0.04	0.286	0.19	0.05

289

290

291

292

293

294

295

296

297

298

Nine samples with saturated 3,550 cm<sup>-1</sup> peaks are excluded.  
 CO<sub>2</sub> and OH<sup>-</sup> were always below detection limit and are thus excluded.

D14c is shown in this table and also in the speciation plot (**Figure 6**) but as only one spectrum was deemed useable (and is suspected of hydration – section 4.3.1) is excluded from reconstructions of palaeo-pressure.

a Single measurement of sample thickness at location (within tens of microns) of FTIR analysis. With the exception of D12a where two locations on the wafer were measured.

b Number of successful FTIR measurements per sample.

c Mean absorbance levels from the 3,550 cm<sup>-1</sup> (total water) and 1,630 cm<sup>-1</sup> (molecular water) peaks.

299 d Mean total ( $H_2O_t$ ) and molecular ( $H_2O_m$ ) water contents calculated using the Beer-Lambert law, assuming a density  
300 of  $2,415 \text{ kg m}^{-3}$  and absorption coefficients of  $80 \text{ l mol}^{-1} \text{ cm}^{-1}$  and  $55 \text{ l mol}^{-1} \text{ cm}^{-1}$  respectively.  
301 e Standard deviation on repeat measurements for total ( $H_2O_t$ ) and molecular ( $H_2O_m$ ) water contents.  
302

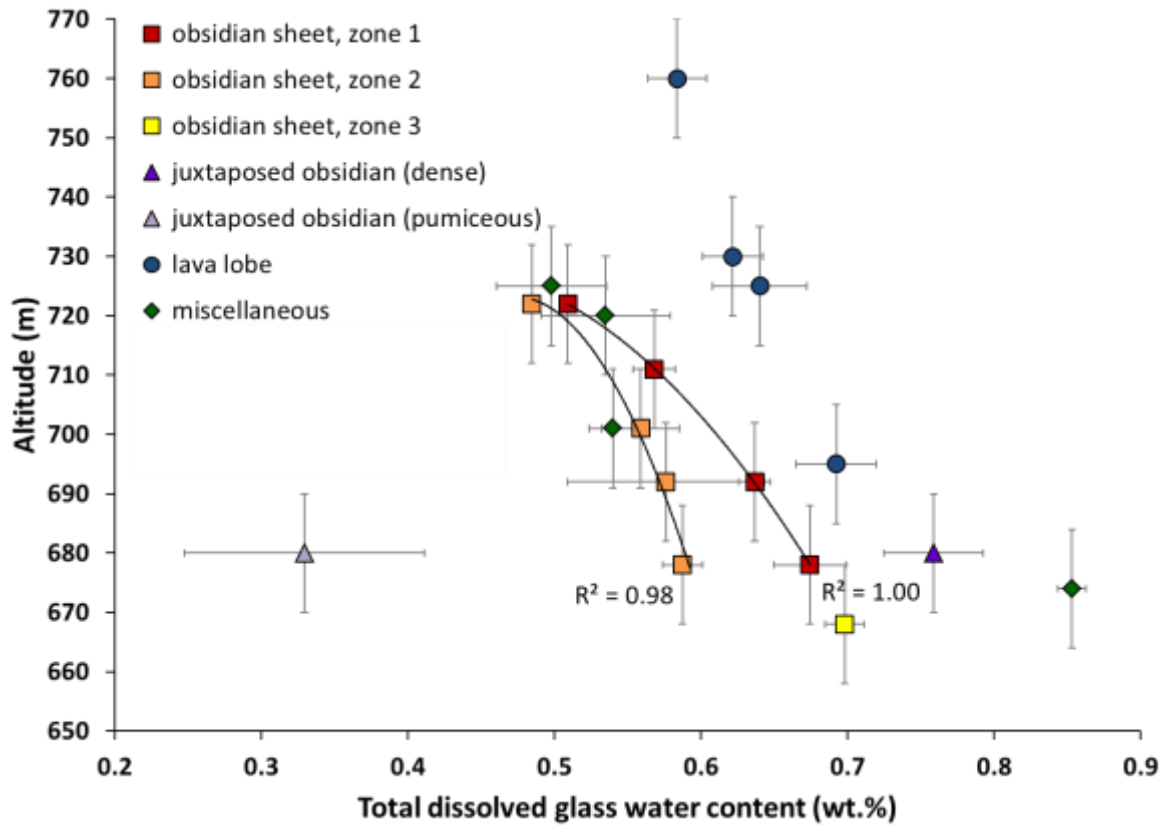
303 Averaged data are shown in **Figure 5**, which is redrawn from Fig. 5 of Owen et al.  
304 (2013b). The water contents of the successfully measured samples (0.33-0.85 wt.%) indicate  
305 partial degassing, consistent with elevated quenching pressures in a subglacial eruption  
306 environment (Tuffen et al., 2010). Initially no systematic relationship between elevation and  
307 water content is evident. However, clear trends emerge when data are grouped by location  
308 and lithofacies type (**Fig. 5**).

309 Water contents from sheet zones 1 and 2 (square symbols) systematically decrease  
310 with elevation, consistent with quenching under a roughly flat-topped ice/water body, with  
311 quenching pressure decreasing with elevation. Zones 1 and 2 are well fitted by simple  
312 polynomial equations. Zone 1 samples are slightly more water-rich, although values converge  
313 at  $\sim 720 \text{ m}$  elevation, indicating underlying complexities that shall be discussed. Lava lobe  
314 water contents (circular symbols) similarly decrease with elevation, but at any given elevation  
315 are more water-rich than the sheets (**Fig. 5**). The pumiceous juxtaposed obsidian is  
316 significantly more degassed than the other samples.

317

318

319



320

321 **Figure 5:** Water content plotted as a function of elevation, modified from Owen et al. (2013b). Symbols  
 322 and colours indicate different lithofacies. Curved lines represent trendlines using a polynomial fit. Each  
 323 data point represents the mean H<sub>2</sub>O concentration from ≥3 analyses, with the standard deviation  
 324 represented by the x-error bars (there is also a 10% error associated with FTIR, however comparative  
 325 error is <3% for typical Dalakvísl samples). The y-error bars represent a ±10 m uncertainty in GPS  
 326 measurements but comparative errors will be much smaller.

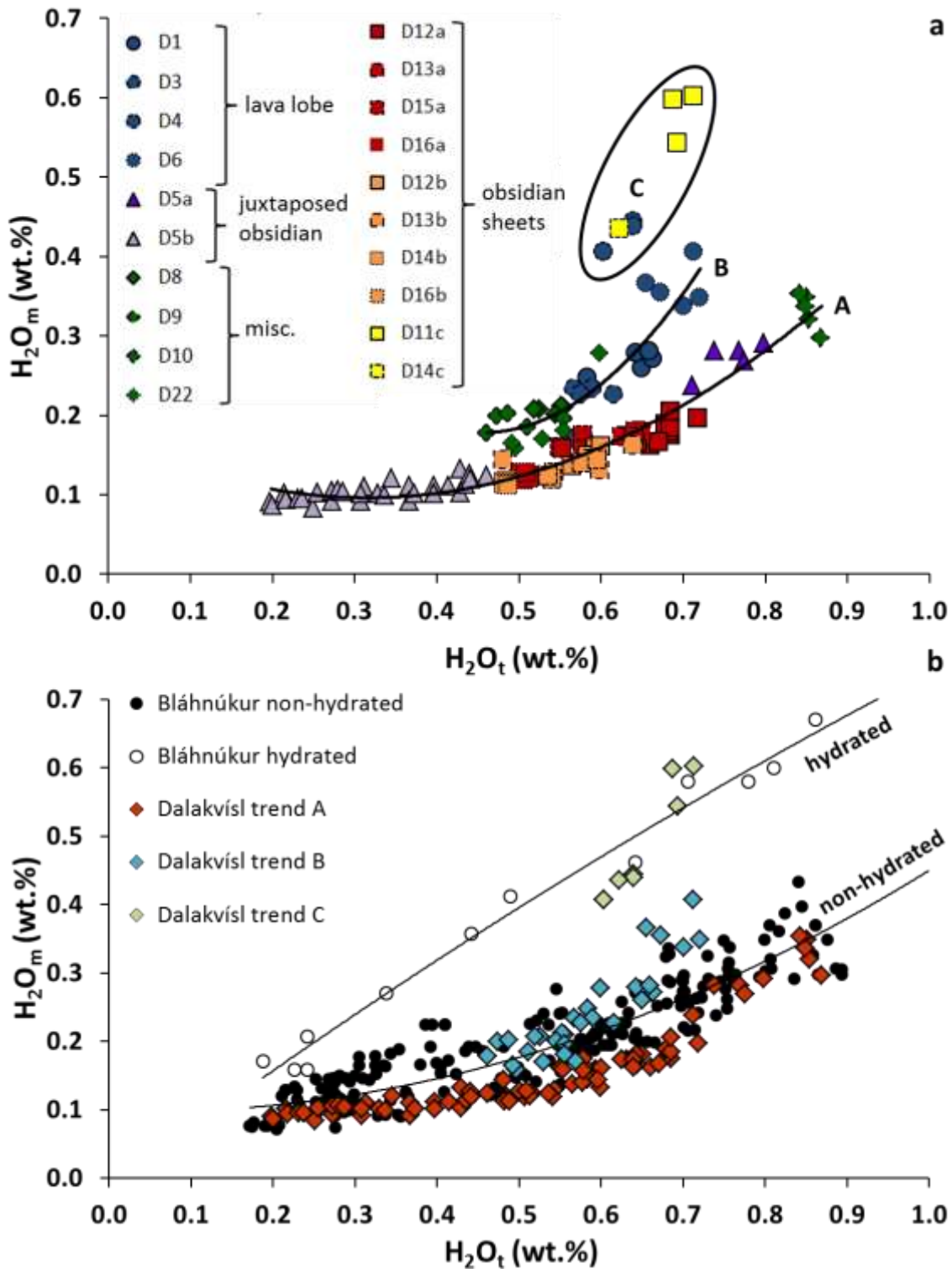
327

#### 328 4.1.1 Water speciation

329 Hydrated samples must be avoided to prevent quenching pressure overestimates  
 330 (Tuffen et al., 2010). Water speciation can indicate whether hydration has occurred as

331 meteoric water is predominantly added in molecular ( $H_2O_m$ ) rather than hydroxyl ( $OH^-$ ) form  
332 (Yokoyama et al., 2008; Denton et al., 2009). Raw speciation data are plotted in **Figure 6**; most  
333 data fit two distinct trendlines, with trendline A encompassing all zone 1 and 2 sheet samples  
334 and with most lava lobe samples falling close to trendline B. Measurements that fit neither of  
335 these trendlines (including all pumiceous zone 3 sheet samples) have exceptionally high ratios  
336 of molecular water (labelled 'C'). These results are discussed in section 4.3.1.

337



338

339 **Figure 6:** FTIR speciation data **(a)** Most of the raw Dalakvísl data lie close to two polynomial trendlines,  
 340 labelled A and B. The circled area C indicates outliers to these trends. **(b)** Dalakvísl data superimposed  
 341 on speciation data from Bláhnúkur (Owen et al., 2012) where the same absorption coefficients were

342 used, making direct comparisons possible. Bláhnúkur samples are readily divisible into non-hydrated  
 343 and hydrated domains, as shown by the trendlines. The Dalakvísl data have been subdivided according  
 344 to trends A, B and C observed in **Figure 6a**. Errors for H<sub>2</sub>O<sub>t</sub> and H<sub>2</sub>O<sub>m</sub> are 10% and 20% respectively,  
 345 although comparative errors will be considerably smaller.

## 346 **4.2 Geochemistry**

347 XRF data confirms that the Dalakvísl samples are rhyolitic in composition and are  
 348 compositionally similar, both in terms of major (**Table 3**) and trace element (**Fig. 7**) chemistry.  
 349 Furthermore, there are strong similarities between the trace element chemistry (**Fig. 7**) of  
 350 Dalakvísl and SE Rauðfossafjöll, which are both ring fracture edifices. However, there is clear  
 351 distinction between Dalakvísl and Bláhnúkur, which formed in separate Torfajökull eruptions  
 352 (**Fig. 1b**). Chemistry therefore concurs with the model that Dalakvísl was monogenetic  
 353 (McGarvie et al., 2007) and concurrent with the SE Rauðfossafjöll eruption (McGarvie et al.,  
 354 2006; Tuffen et al., 2008). The data also suggests that compositional variation was not a factor  
 355 in determining the behavioural changes of the eruption.

356

357 **Table 3:** XRF major and trace element data for four representative samples from Dalakvísl.

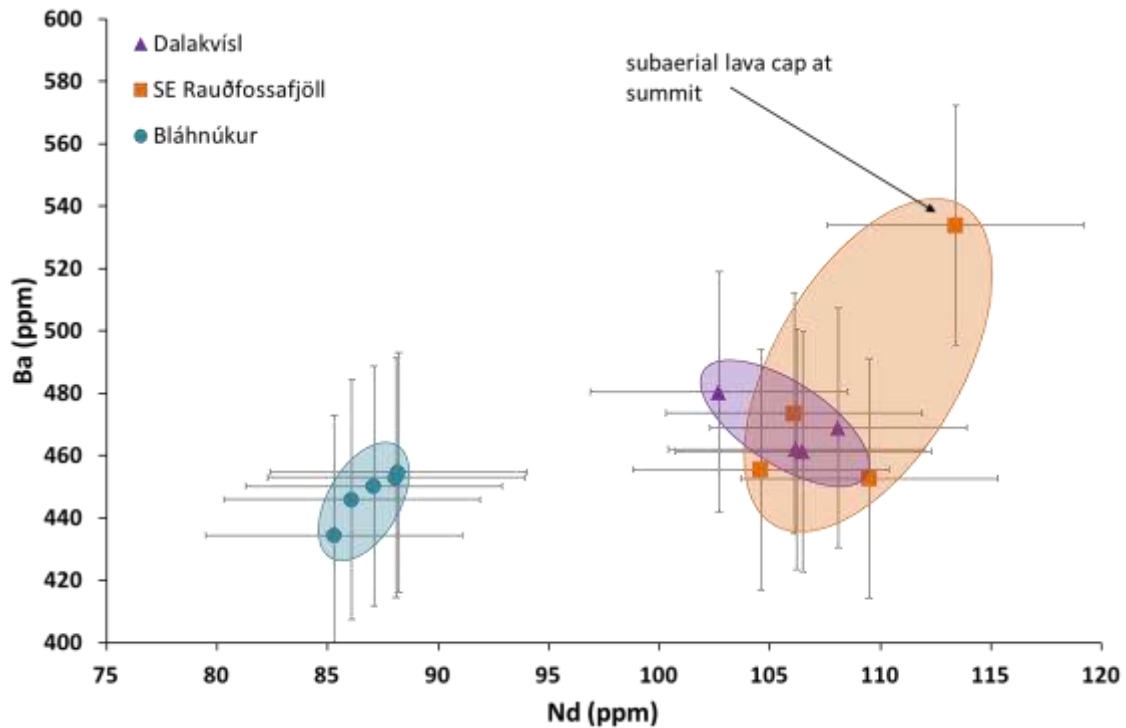
	<b>D1</b>	<b>D7a</b>	<b>D13a</b>	<b>D22</b>	<b>Error</b>
Facies type	Lava lobe	Crudely bedded ash	Obsidian sheet	Miscellaneous	
<b>SiO<sub>2</sub></b>	72.41	70.09	71.40	71.74	0.293
<b>TiO<sub>2</sub></b>	0.42	0.39	0.39	0.39	0.030
<b>Al<sub>2</sub>O<sub>3</sub></b>	13.30	13.12	13.09	13.32	0.270
<b>Fe<sub>2</sub>O<sub>3</sub></b>	2.82	2.23	2.65	2.73	0.157
<b>MnO</b>	0.12	0.10	0.12	0.13	0.004

<b>MgO</b>	0.26	0.20	0.24	0.26	0.207
<b>CaO</b>	0.69	0.59	0.69	0.72	0.190
<b>Na<sub>2</sub>O</b>	5.28	2.99	5.25	5.28	0.253
<b>K<sub>2</sub>O</b>	3.91	4.27	3.86	3.87	0.043
<b>P<sub>2</sub>O<sub>5</sub></b>	0.04	0.03	0.04	0.04	0.021
<b>LOI</b>	0.99	5.67	2.26	0.84	/
<b>Total</b>	100.24	99.66	99.99	99.32	/
<b>Al</b>	0.004	0.035	0.003	0.004	/
<b>ASI</b>	0.94	1.24	0.93	0.94	/
<b>Classification</b>	metaluminous	peraluminous	metaluminous	metaluminous	/
<b>Ba</b>	468.9	480.4	461.3	462.0	38.50
<b>Sc</b>	0.3	1.1	0.9	0.6	2.27
<b>V</b>	1.2	n.d.	n.d.	n.d.	25.23
<b>Cr</b>	n.d.	n.d.	n.d.	n.d.	34.23
<b>Cu</b>	3.0	5.4	4.1	3.3	2.83
<b>Nb</b>	176.7	167.7	175.6	175.5	12.37
<b>Ni</b>	n.d.	n.d.	n.d.	n.d.	14.97
<b>Pb</b>	8.6	8.6	8.2	8.4	7.35
<b>Rb</b>	92.3	106.4	91.7	91.9	6.13
<b>Sr</b>	84.5	93.8	86.4	87.4	12.13
<b>Th</b>	16.2	15.0	16.3	15.9	2.27
<b>U</b>	5.2	4.3	4.9	5.0	0.27
<b>Y</b>	110.9	98.4	107.7	108.0	2.63
<b>Zn</b>	162.2	132.6	148.3	153.8	6.43
<b>Zr</b>	873.0	825.5	871.3	866.5	13.60
<b>La</b>	117.7	113.7	116.1	116.4	4.87
<b>Ce</b>	243.4	234.6	241.2	239.5	11.73
<b>Nd</b>	108.1	102.7	106.5	106.2	5.80

358  
359  
360  
361  
362  
363  
364  
365  
366  
367  
368

Major elements are in wt.% and trace elements are in ppm  
LOI Loss on ignition.  
n.d. not detected.  
Al alkalinity index where  $Al = Al - (K + Na)$  in molecular form;  $Al < 0$  defines peralkaline rocks whereas  $Al > 0$  defines metaluminous and peraluminous rocks (Frost and Frost, 2008).  
ASI aluminum saturation index where  $ASI = Al / (Ca - 1.67P + Na + K)$  in molecular form;  $ASI > 1$  defines peraluminous rocks whereas  $ASI < 1$  are metaluminous or peralkaline (Frost and Frost, 2008).  
Error the maximum difference between the measured and expected values (in wt.% for major elements and ppm for trace elements) of XRF standards.





369

370 **Figure 7:** Trace element (XRF) data for Dalakvísl, SE Rauðfossafjöll and Bláhnúkur; three rhyolitic  
 371 Torfajökull edifices, modified from Owen et al. (2012). Dalakvísl compositions (purple triangles) are  
 372 closely clustered and mostly overlap with SE Rauðfossafjöll (orange squares), but plot separately from  
 373 Bláhnúkur (blue circles). Error bars represent the difference between the measured and expected  
 374 values of standards (**Table 3**).

### 375 **4.3 Removal of data unsuitable for quenching pressure reconstruction**

#### 376 **4.3.1 Hydrated samples**

377 Samples plotting in field 'C' (**Fig. 6a**) have exceptionally high molecular/total water  
 378 ratios, indicative of hydration, and overlap with hydrated samples from Bláhnúkur (**Fig. 6b**).  
 379 Most of these samples are pumiceous and will therefore have a high surface area to volume  
 380 ratio, favouring hydration. These samples are therefore excluded from the final data-set.  
 381 Remaining data overlap with the non-hydrated samples from Bláhnúkur (**Fig. 6b**), thus we can

382 be confident that these samples are non-hydrated due to their relatively low  $H_2O_m : H_2O_t$   
383 ratios.

384 Distinct trendlines A and B (**Fig. 6a**) likely reflect the cooling rate dependence of water  
385 speciation (Stolper, 1982; Ihinger et al., 1999; Xu and Zhang, 2002; Di Muro et al., 2006), with  
386 slower-cooled lava lobe samples plotting at higher molecular/total water ratios (trendline B).  
387 Obsidian sheets, being smaller volume than lava lobes, cooled more rapidly and so have lower  
388 molecular/total water ratios (trendline A).

389

#### 390 *4.3.2 Post-quinching movement*

391 Samples that have travelled downhill (either by flowing, or gravity collapse) may lead  
392 to under-estimations of palaeo-ice thicknesses, as the samples may have degassed at higher  
393 elevation and therefore lower pressure conditions prior to transportation (Moore, 1965;  
394 Macpherson, 1984; Tuffen et al., 2010).

395 Locality D5 consists of juxtaposed domains of obsidian with spatially variable textures,  
396 which are cut by small-scale faults (**Figs. 2ci,ii**). These textures, together with the highly  
397 degassed nature of the pumiceous sample, leads us to suspect this locality has been  
398 remobilised post-quinching, therefore these results are removed from the final data-set.

#### 399 *4.3.3 Equilibrium degassing*

400 Any samples degassed under non-equilibrium conditions will not record their  
401 quenching pressures (Tuffen et al., 2010). As summarised in Rutherford (2008), many  
402 vesiculation-degassing models (e.g. Gardner et al., 1999; Mangan and Sisson, 2000) show that  
403 equilibrium degassing of rhyolite should occur at magma ascent velocities  $<0.7 \text{ ms}^{-1}$ .

404 Estimates of magma ascent velocity at Dalakvísl are 0.001-0.01 ms<sup>-1</sup>, based on inferred  
405 volume fluxes of 5-50 m<sup>3</sup>s<sup>-1</sup> (Tuffen et al., 2007) and a plausible dyke width of 5 m. The  
406 estimated velocity is similar to that estimated for explosive and effusive rhyolitic eruptions at  
407 the Inyo volcanic chain (Castro and Gardner, 2008). Independent estimates using a simple  
408 buoyant magma rise model (Höskuldsson and Sparks, 1997) and plausible dyke dimensions  
409 (1.5 km x 5 m thickness) give a lower value: 0.001 ms<sup>-1</sup>. As both estimates are substantially  
410 lower than the critical ascent velocity of 0.7 ms<sup>-1</sup> (Rutherford, 2008), Dalakvísl magma should  
411 meet the requirements for equilibrium water degassing.

412         Shallow vesiculation during explosive activity can trigger pre-quench acceleration, and  
413 thus it is conceivable that explosively generated material may have briefly exceeded the 0.7  
414 ms<sup>-1</sup> equilibration threshold at shallow conduit depths. However, disequilibrium degassing  
415 reflects the inability of magma degassing to keep track with decompression (Proussevitch and  
416 Sahagian, 1996), hence any samples degassed in disequilibrium ought to be more water-rich  
417 than their effusively erupted, equilibrium-degassed counterparts. As the opposite is true -  
418 explosively generated samples are consistently more degassed than effusively generated  
419 samples - this difference cannot reflect disequilibrium degassing.

420         Due to the above arguments, our samples have likely experienced equilibrium  
421 degassing and are considered suitable for palaeo-quenching pressure reconstruction.  
422 Furthermore, where samples fit well to a solubility pressure curve, degassing was arguably in  
423 equilibrium. Samples that deviate from expected water-elevation trends could have  
424 undergone disequilibrium degassing, as discussed below.

425

426 4.3.4 The final data-set of samples suitable for reconstructing palaeo-ice thickness

427 With the removal of hydrated (D4, D11c and D14c) and remobilised (D5a and D5b)  
 428 samples, 15 samples remain suitable for palaeo-quenching pressure reconstruction (**Table 4**).

429

430 **Table 1:** Evidence for the Dalakvísl samples meeting the five criteria (Tuffen et al., 2010) needed to  
 431 reconstruct ice thicknesses.

Criterion	Evidence to look for	Evidence at Dalakvísl	Is the criterion met?
<b>Volatile saturation has been reached</b>	The presence of vesicles indicates that some degassing has taken place and therefore the point of volatile saturation must have been reached <sup>a,b</sup>  A negative relationship between elevation and water content is also evidence that degassing has taken place <sup>c</sup>	All but two samples (D10 & D22) have vesicles present.  All samples show decreasing water contents with elevation when viewed within categories ( <b>Fig. 5</b> )	Yes
<b>Degassing was in equilibrium</b>	Equilibrium degassing should be achieved if the ascent rate was $< 0.7 \text{ ms}^{-1}$ <sup>d</sup>	Eruption models suggest an eruption rate of $5\text{-}50 \text{ m}^3\text{s}^{-1}$ , equating to a rise speed of $\sim 10^{-2}$ to $10^{-3} \text{ ms}^{-1}$ along a dyke 1.5 km long and 5 m wide <sup>g,h</sup>	Yes
<b>Homogenous samples</b>	Avoidance of complex textures and similarity between analysis of multiple data points within the same sample <sup>a</sup>	Most of the samples express a small standard deviation as shown by <b>Figure 5</b> and <b>Table 2</b>	Yes
<b>No post-quenching movement</b>	Field evidence <sup>a</sup>	Only two samples were collected from lava bodies that showed evidence of reworking (D5a & D5b; <b>Figs. 2ci,ii</b> ) and these data have been removed	Yes

No post-  
quenching  
hydration

Perlittisation textures and high  
ratios of molecular water<sup>a,e,f</sup>

Three samples (D4, D11c &  
D14c) showed evidence of  
hydration (**Fig. 6**); these have  
been removed

Yes

---

432

433  
434

a=(Tuffen et al., 2010); b=(Höskuldsson et al., 2006); c=(Dixon et al., 2002); d (Rutherford, 2008); e = (Yokoyama et al., 2008); f = (Denton et al., 2009); g = (Tuffen et al., 2007); h = (Höskuldsson and Sparks, 1997)

## 435 **5 Discussion**

### 436 ***5.1 Solubility pressure curves to estimate ice loading***

437 In a monogenetic subglacial eruption, dissolved magmatic water contents typically  
438 decrease with elevation (Dixon et al., 2002; Höskuldsson et al., 2006; Schopka et al., 2006;  
439 Edwards et al., 2009) as edifice construction leads to lower pressure from overlying ice.  
440 Pressure (P in Pa) can be estimated using the formula:

441

$$442 \quad P = \rho gh \quad \text{Equation 2}$$

443 where  $\rho$  is density of overlying material (in  $\text{kg m}^{-3}$ ),  $g$  is gravitational acceleration ( $9.81$   
444  $\text{m s}^{-2}$ ), and  $h$  = thickness of overlying material (in m).

445 Pressures were converted into  $\text{H}_2\text{O}$  contents using the solubility model VolatileCalc  
446 (Newman and Lowenstern, 2002), assuming 0 ppm of  $\text{CO}_2$  and a magma temperature of 800  
447  $^\circ\text{C}$ , to comply with Fe-Ti oxide geothermometry estimates of 750-800  $^\circ\text{C}$  for Torfajökull  
448 rhyolites (Gunnarsson et al., 1998). Note that  $>0$  ppm of  $\text{CO}_2$  and higher magma temperatures  
449 lead to higher quenching pressures for the same dissolved water concentration (Tuffen et al.,  
450 2010).

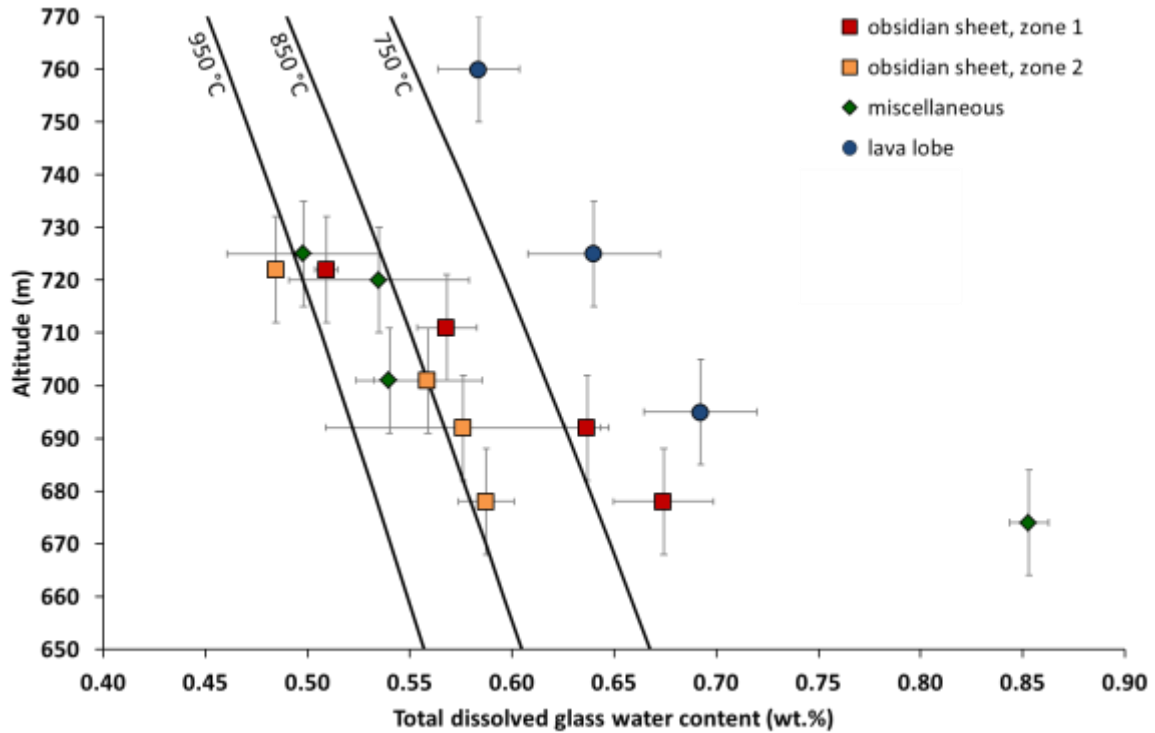
451 By combining the above, we could plot expected water content as a function of  
452 elevation for various loading scenarios. Note that although, these points are an expression of

453 water solubility as a function of depth/elevation, we chose to call the resulting curve a  
454 'solubility pressure curve' (SPC) as ultimately the values are based on solubility-pressure  
455 relationships and this term is consistent with other studies that are pertinent to this paper  
456 (Tuffen et al., 2010; Owen et al., 2012; Owen et al., 2013b; Owen, 2016). A SPC marks the  
457 water content expected at each elevation for a given thickness of overlying ice, meltwater or  
458 rock (Schopka et al., 2006; Tuffen et al., 2010; Owen et al., 2012).

459 A number of different SPCs can be fitted to the Dalakvísl data, suggesting that different  
460 parts of Dalakvísl experienced different conditions that affected water solubility or magma  
461 degassing processes. Water solubility in silicic melt is principally affected by magma  
462 composition, temperature, CO<sub>2</sub> content and pressure (Newman and Lowenstern, 2002).  
463 Neither the measured subtle variation in sample composition (**Fig. 7**), nor plausible variations  
464 in magmatic temperature (**Fig. 8**), can sufficiently influence water solubility to explain the  
465 measured spread of water content-elevation values.

466

467



468

469 **Figure 8:** Measured magmatic water content-elevation relationships (symbols), with a range of  
 470 modelled solubility pressure curves (SPCs), which represent different erupted temperatures (all  
 471 assuming a glacier surface at 1000 m a.s.l. and loading by ice alone).

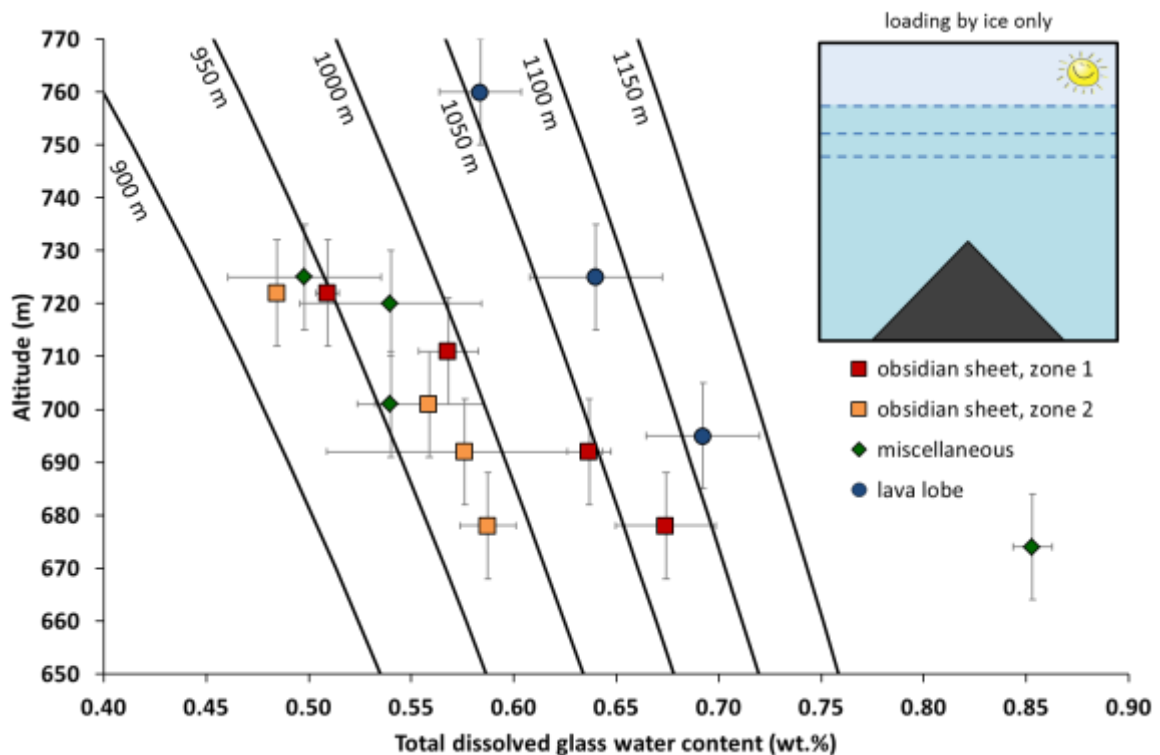
472

473 It is possible that variation in CO<sub>2</sub> content could affect H<sub>2</sub>O solubility-pressure relations  
 474 (Tuffen et al., 2010), but FTIR data indicate CO<sub>2</sub> concentrations <30 ppm. Mixed H<sub>2</sub>O-CO<sub>2</sub>  
 475 degassing models (Owen, 2013), based on calculations in VolatileCalc (Newman and  
 476 Lowenstern, 2002), indicate maximum plausible quenched CO<sub>2</sub> contents of 8 ppm and 5 ppm  
 477 for the least and most degassed obsidian sheets respectively and 0 ppm in the lava lobes. This  
 478 assumes closed and open system degassing for the obsidian sheets and lava lobes  
 479 respectively, and is based upon their pre-eruptive H<sub>2</sub>O concentrations (Owen et al., 2013a;  
 480 Owen et al., 2013b). An 8 ppm variation in CO<sub>2</sub> content is insufficient to explain the H<sub>2</sub>O  
 481 variation observed between the lava lobe and obsidian sheet samples (Owen et al., 2012). It  
 482 is also unlikely that 8 ppm CO<sub>2</sub> remains as this would have required a completely closed

483 system with a high percentage of exsolved vapour (Newman and Lowenstern, 2002) which is  
484 inconsistent with observed vesicularities (Owen et al., 2013b). Thus, we attribute distinct  
485 water solubility-elevation relationships to differences in quenching pressure, which may  
486 reflect different thicknesses/depths of overlying ice, meltwater and/or erupted deposits, or  
487 different subglacial pressure conditions.

488 If loading were by ice alone, a 150 m variation in ice thickness (950 to 1100 m ice  
489 surface elevation) is needed to explain the measured water content range (**Fig. 9**). The upper  
490 value of 1100 m is close to ice surface elevation estimates from subglacial-to-subaerial  
491 lithofacies transitions at nearby, contemporaneously generated ring fracture tuyas (McGarvie  
492 et al., 2006). However, models of loading by ice alone (density  $917 \text{ kg m}^{-3}$ ) produce SPCs that  
493 are too steep to fit the data (**Fig. 9**), suggesting that a higher-density loading medium is  
494 required.

495



496



497 **Figure 9:** Measured magmatic water content-elevation relationships (symbols), with a range of  
498 modelled solubility pressure curves (SPCs), which represent different amounts of ice loading (all  
499 assuming a magma temperature of 800 °C and loading by ice alone). The inset (see legend in Figure  
500 13) illustrates this modelled scenario for Dalakvísl (dark grey triangle), with dashed lines representing  
501 various options for ice surface elevation.

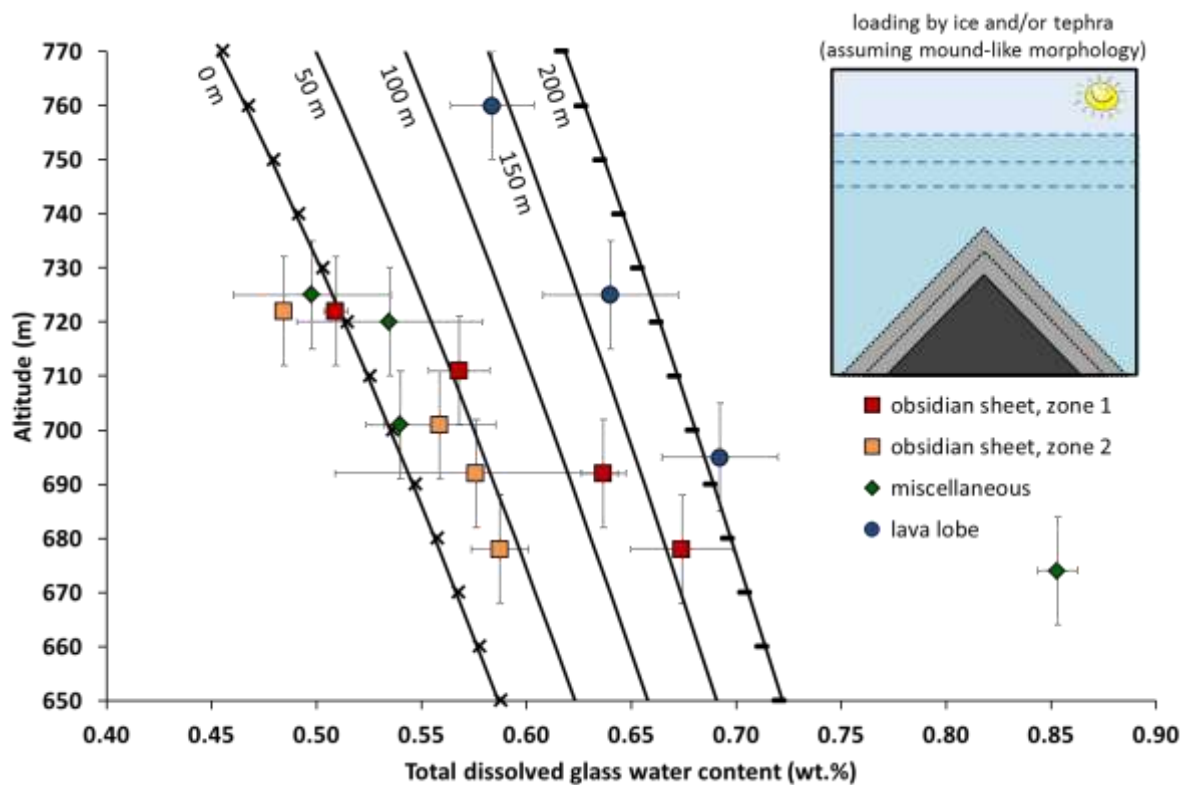
502

## 503 ***5.2 The necessity of loading from fragmental material***

504 The strong decrease in measured water content with elevation (**Fig. 9**) requires either  
505 loading by a higher-density medium than ice or a systematic additional decrease in pressure  
506 with elevation. Indeed, field evidence suggests some Dalakvísl lithofacies formed intrusively  
507 within juvenile pyroclastic deposits, consistent with a component of loading by fragmental  
508 deposits (Tuffen et al., 2008). The density of fragmental material at Dalakvísl is estimated at  
509 1,620 kg m<sup>-3</sup>, i.e. 85% that of basaltic hyaloclastite (Höskuldsson and Sparks, 1997; Tuffen and  
510 Castro, 2009; Owen et al., 2012).

511 SPCs are displayed consistent with loading by fragmental deposits and with two end-  
512 member edifice morphologies – a steep-sided mound similar to the current Dalakvísl  
513 morphology (**Fig. 10**) and a flat-topped edifice similar to a tuya (**Fig. 11**). We prefer the flat-  
514 topped model (**Fig. 11**), which provides a superior data fit compared to the mound model (**Fig.**  
515 **10**), and in fact allows for distinct SPCs to be matched to specific lithofacies.

516

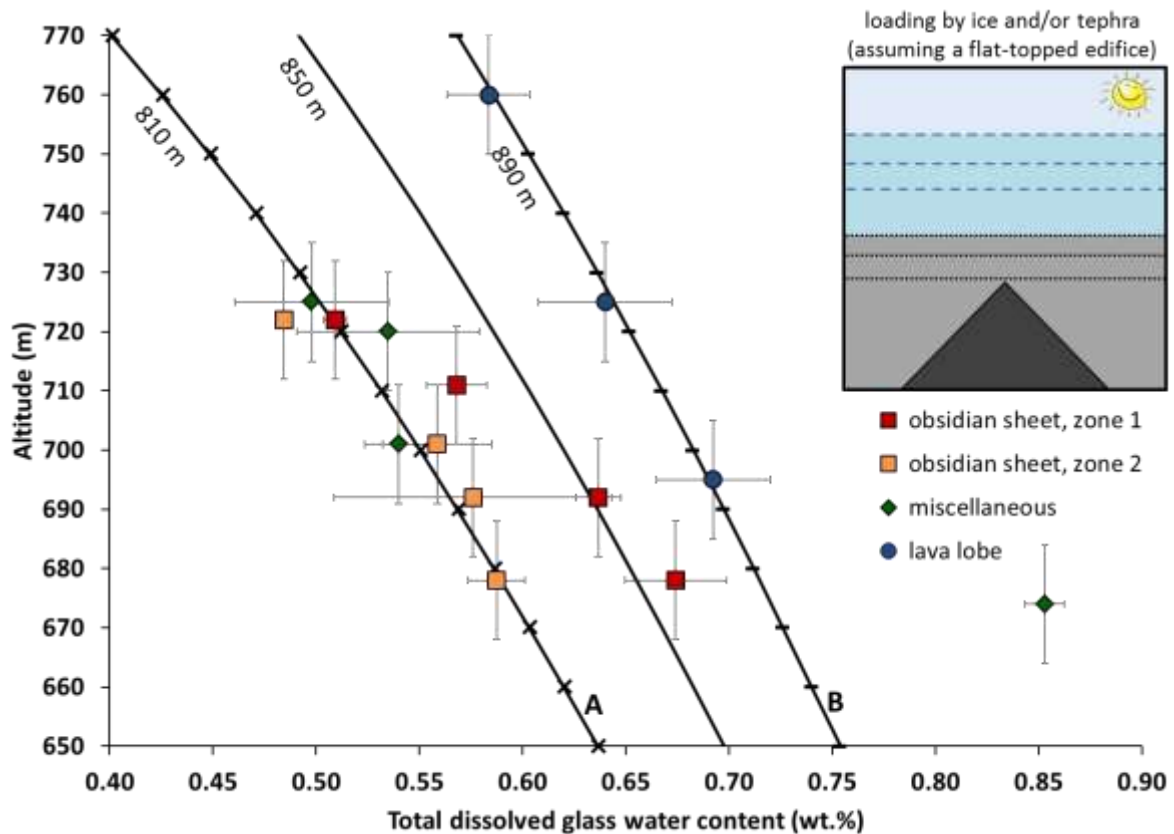


517

518 **Figure 10:** Measured magmatic water content-elevation relationships (symbols), with a range of  
 519 modelled solubility pressure curves (SPCs), which represent different amounts of loading by ice and/or  
 520 overlying fragmental material, assuming a similar mound-like morphology to Dalakvísl today. The  
 521 labels at the top of each SPC indicate the thickness of fragmental material required for a 950 m ice  
 522 surface. Alternatively, the SPCs could represent a change in ice elevation with constant tephra loading.  
 523 For example, for loading by 100 m of fragmental material, the crossed and dashed SPCs could  
 524 represent ice up to 875 m and 1,025 m a.s.l. respectively. The inset illustrates this modelled scenario  
 525 for Dalakvísl (dark grey triangle), with dashed and dotted lines representing various options for ice  
 526 surface elevation and original edifice size, respectively, see also legend in Figure 13.

527

528



529

530 **Figure 11:** Measured magmatic water content-elevation relationships (symbols), with a range of  
 531 modelled solubility pressure curves (SPCs), which represent different amounts of loading by ice and/or  
 532 overlying fragmental material, assuming a flat-topped edifice morphology. The labels at the top of  
 533 each SPC indicate various options for the surface elevations of fragmental material (i.e. edifice summit  
 534 elevations) assuming that it was overlain by 70 m of ice. Alternatively, the SPCs could represent a  
 535 constant edifice height with varying ice thicknesses. For example, assuming loading by fragmental  
 536 material up to 850 m a.s.l., the crossed and dashed SPCs (labelled A and B respectively for reference  
 537 in the text) could represent additional ice loading of 0 and 140 m respectively. The inset illustrates this  
 538 modelled scenario for Dalakvísl (dark grey triangle), with dashed and dotted lines representing various  
 539 options for ice surface elevation and original edifice size, respectively, see also legend in Figure 13.

540

541 In **Figure 11** the majority of the data fits to two SPCs – a high pressure SPC (B) fits the  
 542 lava lobe samples and a lower pressure SPC (A) fits zone 2 sheet samples and the majority of

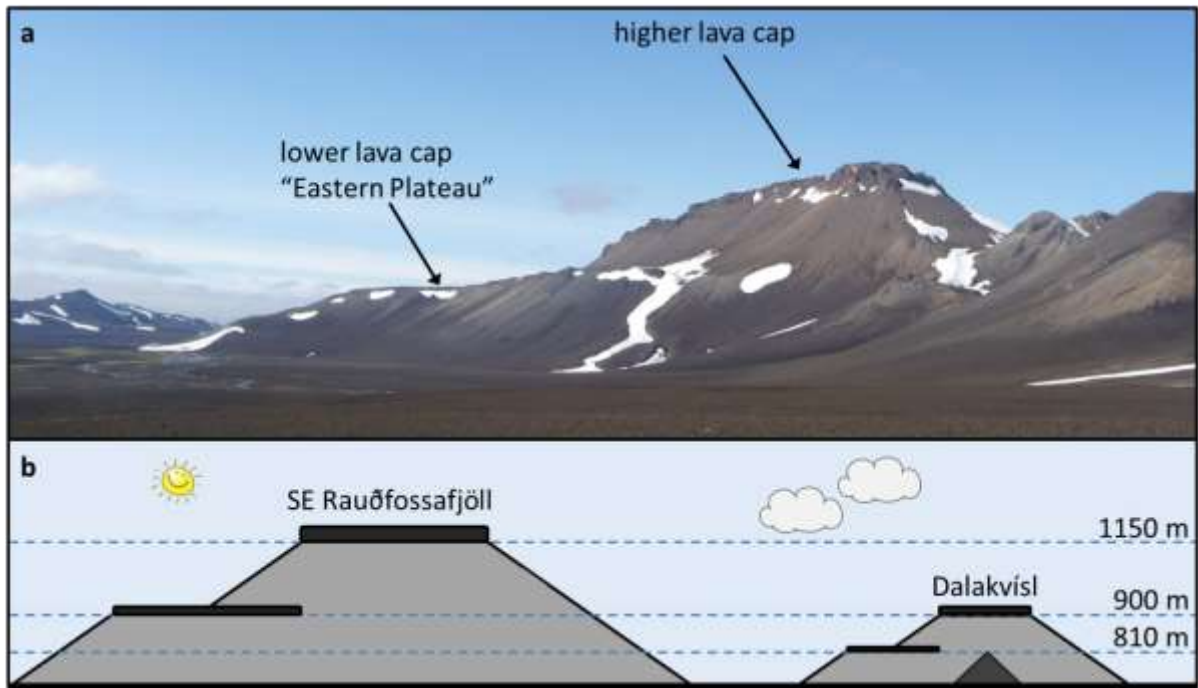
543 the samples labelled 'miscellaneous'. Zone 1 sheet samples plot between SPCs A and B but  
544 merge towards SPC A as elevation increases. Only one sample, D9 (from a poorly exposed  
545 obsidian mound), is anomalous (with ~0.85 wt.% H<sub>2</sub>O). The excellent fit of the SPCs in **Figure**  
546 **11** to the data is consistent with an originally flat-topped edifice, suggesting that all samples  
547 formed intrusively and quenched within fragmental deposits. The marked difference between  
548 the water content of sheet and lava lobe samples probably reflects spatial and/or temporal  
549 differences in overlying ice thickness, meltwater pressure and/or the height of the overlying  
550 edifice, as will be discussed.

### 551 **5.3 Did Dalakvísl erupt as a tuya?**

552 As the best-fitting SPCs require that Dalakvísl was erupted as a flat-topped edifice (**Fig.**  
553 **11**), was it originally a tuya? Loading by a 27 m thick rhyolitic lava cap (density 2,415 kg m<sup>-3</sup>)  
554 could replace the loading by 70 m of ice in **Figure 11**. As two distinct SPCs fit the majority of  
555 the data (**Fig. 11**), these could be explained by a double-tiered tuya (similar to SE  
556 Rauðfossafjöll, (Tuffen et al., 2002); **Fig. 12a**), with summits at 837 m and 917 m respectively.  
557 In this case, perlitised lava on the summit of Dalakvísl (Tuffen et al., 2008) could represent the  
558 now-eroded base of a lava cap; its elevation correlates well with the inferred lava cap height  
559 inferred from SPC A (**Figs. 11, 12a**). The elevation of the inferred lava cap for SPC B is higher  
560 than the preserved Dalakvísl deposits, instead matching that of the lower lava cap of SE  
561 Rauðfossafjöll (Eastern Plateau) (**Fig. 12**), thought to have erupted contemporaneously with  
562 Dalakvísl (Tuffen et al., 2008).

563

564



565

566 **Figure 12: (a)** SE Rauðfossafjöll, a tuya formed contemporaneously to Dalakvísl, viewed from the east.

567 **(b)** Schematic representations of SE Rauðfossafjöll (left) and a plausible original morphology of

568 Dalakvísl (right), with the current morphology represented by the dark grey triangle. Dark rectangles

569 represent subaerial lava caps and pale grey represents subglacially produced deposits. The blue

570 dashed lines show inferred paleo-ice thicknesses, see also legend in Figure 13.

571

572 The tuya model presented in **Figure 12** suggests a minimum of three ice levels during the

573 eruption of the ring fracture rhyolites: two for Dalakvísl and two for SE Rauðfossafjöll, with

574 the higher Dalakvísl ice surface and the lower SE Rauðfossafjöll ice surface being similar. The

575 trace element concentrations of samples from Dalakvísl and the lower part of SE

576 Rauðfossafjöll overlap (**Fig. 7**), with only the upper lava cap sample from SE Rauðfossafjöll

577 having anomalous Ba contents. The Eastern Plateau and Dalakvísl may have therefore erupted

578 together when ice surface elevation was ~900 m a.s.l., with the higher lava cap at SE

579 Rauðfossafjöll erupting at a different time when the ice was thicker. This is consistent with  
580 the proposal that the ring fracture rhyolites erupted during multiple but closely spaced events  
581 over an 800 year period (Brendryen et al., 2010). However, substantial erosion from Dalakvísl  
582 is required to completely remove the second lava cap at ~900 m, plus >80 m of fragmental  
583 deposits, to produce today's topography. Dalakvísl's position at a comparatively low elevation  
584 at the margin of the subglacially erupted Rauðfossafjöll massif (**Fig. 1b**) could make it  
585 particularly susceptible to erosion from eruption-triggered meltwater and during subsequent  
586 deglaciation (indeed rivers are still present today; **Figure 3**). However, it is also notable that  
587 this tuya model cannot explain the variation in vesicularity (Owen et al., 2013b) or H<sub>2</sub>O  
588 contents (**Fig. 5**) found within the obsidian sheets. Therefore, we shall also consider  
589 alternative models.

#### 590 ***5.4 Constraining syn-eruptive ice surface elevation***

591 The tuya model suggests palaeo-ice thicknesses at ca. 810 m and 900 m, consistent  
592 with perlitised lava on the summit of Dalakvísl, and the elevation of the Eastern Plateau,  
593 respectively. However, we must also consider the possibility that the eruption was entirely  
594 subglacial and a lava cap never formed. SPCs A and B in **Figure 11** fit well with the water data,  
595 but we cannot directly convert loading pressures into ice thicknesses because the SPC  
596 gradients require some loading by fragmental material. Each SPC represents a range of  
597 potential ice thicknesses, coupled with various potential amounts of fragmental material. We  
598 can, however, constrain this range by assuming: (1) the edifice was flat-topped during the  
599 eruption and its surface elevation was  $\geq 810$  m (**Fig. 11**), i.e. the summit elevation today; (2)  
600 the densest loading material was fragmental deposits ( $1,620 \text{ kg m}^{-3}$ ); (3) the loading material

601 with the lowest density was ice ( $917 \text{ kg m}^{-3}$ ); and (4) quenching pressure was equal to  
 602 lithostatic/glaciostatic pressure.

603 For each of the two well-fitted SPCs in **Figure 11** we have thus estimated a minimum  
 604 and a maximum ice surface level by applying the highest and lowest possible ratios of  
 605 fragmental material to ice respectively (**Table 5**). It is highly probable that meltwater was also  
 606 present as a loading material but this does not affect the minimum and maximum values as  
 607 water density ( $1000 \text{ kg m}^{-3}$ ) falls between that of ice and hyaloclastite.

608

609 **Table 2:** Minimum and maximum ice surfaces estimated for solubility pressure curves A and B in **Figure**  
 610 **11**.

	SPC A	SPC B
Minimum edifice level (m a.s.l.)	810	810
Therefore maximum ice thickness (m)	70	210
Therefore maximum ice surface (m a.s.l.)	880	1,020
Minimum ice thickness (m)	0	0
Therefore maximum edifice level (m a.s.l.)	850	930
Therefore minimum ice surface (m a.s.l.)	850	930

611

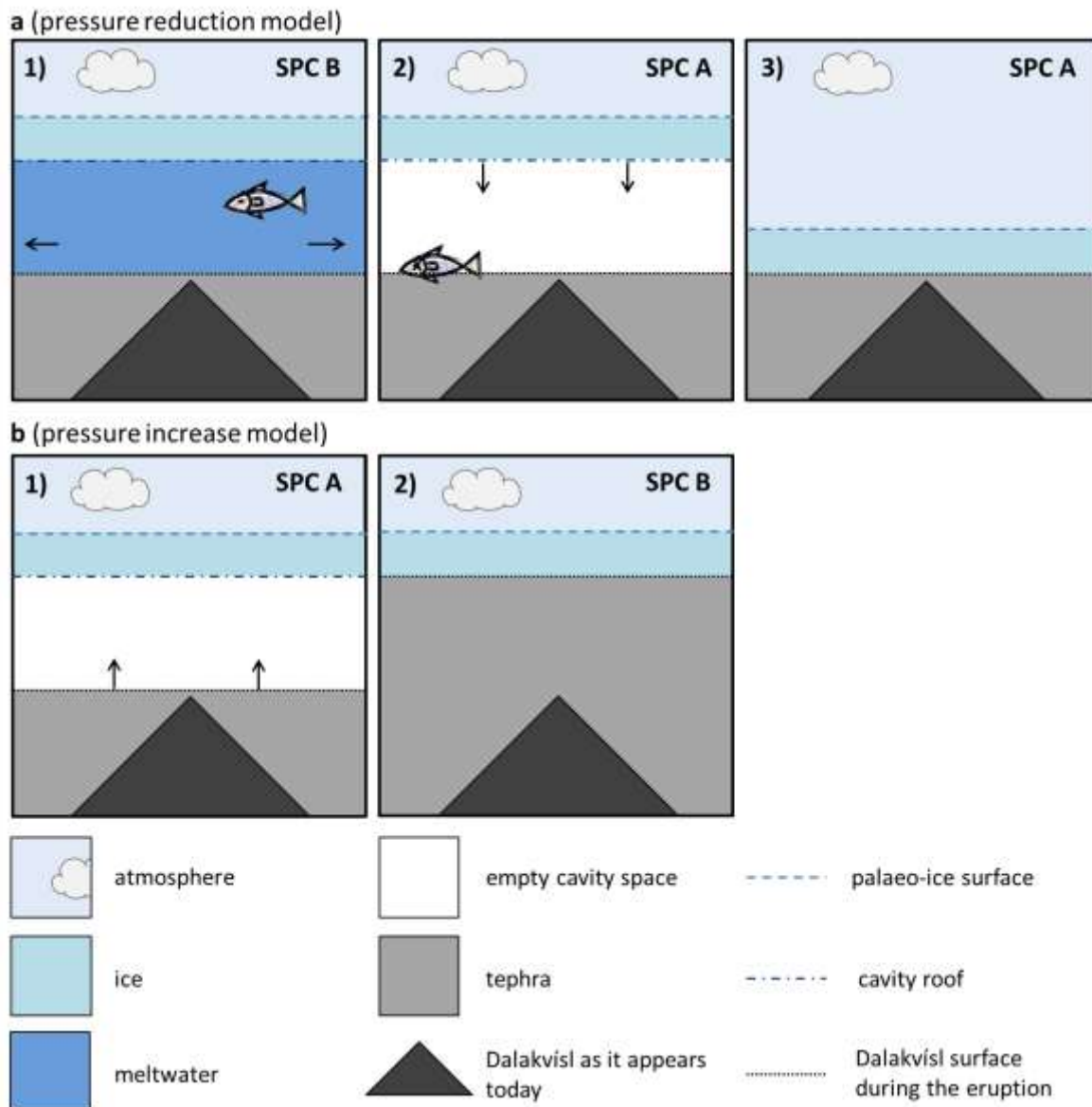
612 As shown by **Table 5**, the implied ice surface level during the construction of the zone  
 613 2 sheet samples (SPC A) was 850-880 m a.s.l., whereas the lava lobes (SPC B) correspond with  
 614 an ice surface of 930-1,020 m a.s.l. The maximum ice thickness was 70 and 210 m for SPCs A  
 615 and B respectively. There is no overlap between the two suggested ranges in **Table 5**. One  
 616 potential explanation is that a significant time gap existed between the formation of samples  
 617 falling on SPCs A and B (**Fig. 11**) so that different ice surface levels could develop. However,

618 changing subglacial pressure and under-pressured cavities are attractive alternative  
619 scenarios, as discussed below.

### 620 ***5.5 Two models for the order of events***

621 **Figure 11** suggests that effusive lava lobe-forming activity was associated with higher  
622 quenching pressure than more explosive obsidian sheet production. Therefore, the transition  
623 in style was either effusive to explosive, associated with a pressure reduction (**Fig. 13a**) e.g.  
624 by meltwater drainage (Owen et al., 2013b), or explosive to effusive and associated with a  
625 pressure increase (**Fig. 13b**), e.g. by increasing load of overlying tephra (Tuffen et al., 2007;  
626 Tuffen et al., 2008).





627

628 **Figure 13:** Schematic illustrations showing potential models for the order of events at Dalakvísl. **(a)** An  
 629 initially water-filled cavity (1) drains, leading to pressure reduction; the cavity may be temporarily air-  
 630 filled (2) prior to cavity closure by ice deformation (3). **(b)** An air-filled cavity (1) becomes tephra-filled,  
 631 increasing confining pressure (2). Corresponding SPCs from **Figure 11** are indicated in each panel.

632

633 The pressure reduction model (**Fig. 13a**) requires the effusive lava lobes to form first  
 634 (SPC B), followed by more explosive activity under a lower confining pressure regime (SPC A).

635 The most likely reason for a pressure reduction during a subglacial eruption is ice melting and  
636 meltwater drainage, suggesting that SPC B represents loading from a large column of  
637 ice/meltwater, whereas SPC A represents a time when the ice was much thinner and after  
638 meltwater has drained. The inferred pressure difference between SPCs A and B in **Figure 11**  
639 is 1.3 MPa. If exclusively due to meltwater drainage, this corresponds to a water level change  
640 of 130 m, which is plausible considering there was a 170-180 m drop in the Grímsvötn lake  
641 level during the 1996 Gjalp eruption (Guðmundsson et al., 2004). This pressure reduction  
642 model is still compliant with a palaeo-ice surface elevation of up to 1,020 m, as suggested in  
643 **Table 5**, which is similar to independent elevation estimates for neighbouring ring-fracture  
644 tuyas thought to have erupted contemporaneously with Dalakvísl (McGarvie et al., 2006).  
645 Furthermore, abundant <10 µm spherical bubbles within sheet cores (zone 1) are attributed  
646 to rapid decompression followed by immediate quenching (Sparks and Brazier, 1982; Larsen  
647 and Gardner, 2000; Höskuldsson et al., 2006; Stevenson, 2011; Owen et al., 2013b). The  
648 variation in H<sub>2</sub>O content observed in the obsidian sheets (e.g. **Fig. 5**) is also consistent with  
649 rapid decompression.

650 The pressure increase model (**Fig. 13b**) requires initial lower-pressure explosive  
651 activity (SPC A), followed by effusive activity (SPC B) under higher confining pressure.  
652 Increased confining pressure may reflect a thickening accumulation of overlying pyroclastic  
653 debris (Tuffen et al., 2007) or blockage of meltwater drainage and subsequent pressure  
654 increase. In closed subglacial systems, the low heat content of rhyolite, in comparison to  
655 basalt, results in insufficient ice melting to accommodate the volume of the erupted deposits  
656 (Höskuldsson and Sparks, 1997). Thus, if meltwater is unable to drain, confining pressure will  
657 increase and over-pressure will develop.

658 Tuffen et al (2008) proposed that the obsidian sheets were emplaced as a foam, which  
659 collapsed pre-quenching due to a pressure increase, driving volatile resorption in dense sheet  
660 cores to give higher water concentrations than corresponding sheet margins. However,  
661 vesiculation-degassing modelling suggests that the difference in H<sub>2</sub>O content between  
662 obsidian sheet zones exceeds that produced by bubble collapse and resorption alone (Owen  
663 et al., 2013b). Additionally, the rapid decrease in sheet core water contents with increasing  
664 elevation (e.g. **Fig. 11**) cannot be explained with this model. Finally, a lack of bubble collapse  
665 features and an abundance of ‘decompression bubbles’ within sheet cores means that vesicle  
666 textures are more consistent with rapid depressurisation rather than pressure increase (Owen  
667 et al., 2013b).

668 The pressure reduction model is also more consistent with independent palaeo-ice  
669 reconstructions. Problematically, both the pressure increase model and the tuya model  
670 require a significant contribution of loading from fragmental material with considerably  
671 higher density than meltwater/ice. The knock-on modelling effect is to require far lower  
672 palaeo-ice thicknesses (**Table 5**), which are inconsistent with independent estimates. Also,  
673 the strong presence of columnar-jointed obsidian, perlite, and blocky ash shards all suggest that  
674 there was abundant meltwater present during the eruption.

675 Considering all the arguments laid out in this section, we favour the pressure  
676 reduction model, with an initial palaeo-ice surface elevation close to 1,020 m.

677 Furthermore, the evidence suggests that the pressure reduction was a rapid  
678 decompression event, most likely triggered by a syn-eruption jökulhlaup. This best explains  
679 the variation in H<sub>2</sub>O contents, vesicularities and vesicle textures of the obsidian sheets. Owen  
680 et al. (2013b) propose that a syn-eruptive jökulhlaup caused a sudden and rapid vesiculation  
681 event within the obsidian sheet deposit, which was being emplaced at the time. In the sheet

682 margins, short diffusion distances (caused by localised shearing) permitted a rapid degassing  
683 response to the change in confining pressure, allowing existing vesicles to grow and the sheet  
684 margins to froth up. Degassing could keep pace with the pressure change, hence why these  
685 samples plot to a SPC (**Fig. 11**). However, negligible degassing took place in the dense sheet  
686 cores. Diffusion distances were too large, thus the magma responded by nucleating new  
687 bubbles, which did little to deplete the melt in volatiles. Essentially, these samples are  
688 recording non-equilibrium degassing following the pressure drop (hence not fitting to a SPC).  
689 The deviation of the zone 1 sheet samples from SPC A therefore represents the degree of  
690 disequilibrium. This decreases with elevation (**Fig. 11**), presumably as the jökulhlaup was  
691 coming to an end and degassing could more easily keep pace with changing pressure.

692 It is unlikely that the jökulhlaup completely drained the subglacial cavity as  
693 establishment of a hydrological connection with the glacier snout will result in degassing to  
694 atmospheric conditions (Hooke, 1984) whereas as all samples are recording elevated H<sub>2</sub>O  
695 concentrations (e.g. **Fig. 5**).

## 696 ***5.6 Defining the syn-eruptive ice thickness***

697 Assuming that SPC B represents the first phase of the eruption, an initial palaeo-ice  
698 surface between 930 and 1,020 m is required (**Table 5**). The higher end is close to inferred  
699 palaeo-ice surface elevations of 1,093 m and 1,087 m from subglacial-subaerial lithofacies  
700 transitions at the contemporaneous ring fracture edifices Illihnúkur and SW Rauðfossafjöll,  
701 respectively (McGarvie et al., 2006). As the current base of Dalakvísl is ~670 m a.s.l. (**Fig. 3**),  
702 this suggests a syn-eruptive ice thickness of ~350 m a.s.l., which is also in agreement with the  
703 ice thickness inferred by Tuffen et al. (2008).

704 Note that this inferred palaeo-ice thickness is based on SPC B which has been fitted to  
705 the effusive lava lobe samples. Owen et al. (2013a) and Owen et al. (2013b) speculate that  
706 effusive parts of Dalakvísl erupted under conditions of open-system degassing, which should  
707 have completely degassed in CO<sub>2</sub> (Owen, 2013), thus we can be confident that residual CO<sub>2</sub>  
708 will not be affecting the reconstructed ice thickness.

709 We speculate that the ice melted but drainage was hindered (Tuffen et al., 2008) until  
710 a jökulhlaup rapidly relieved pressure (Owen et al., 2013b), resulting in a new ice surface at  
711 ~880 m a.s.l. (**Table 5**). This modelling assumes 0 ppm of CO<sub>2</sub>, but it is possible that up to 8  
712 ppm of CO<sub>2</sub> remains in the obsidian sheets (Owen, 2013). However we think this unlikely due  
713 to evidence of late stage open-system degassing (Owen et al., 2013b) and the good fit of our  
714 data to the SPCs in **Figure 11**.

715

## 716 ***5.7 Defining the original edifice size and morphology***

717 We hypothesise that the eruption constructed a near-horizontal edifice top at ~810 m  
718 a.s.l, above fragmental deposits, with an initial ice surface elevation at ~1,020 m (**Table 5, Fig.**  
719 **11**). In this case, insignificant erosion has since occurred from the edifice top (current summit  
720 elevation ~810 m), but substantial erosion (up to 140 m) has occurred from the edifice  
721 margins to produce today's mound-like shape. This is consistent with the presence of perlitic  
722 lava at the Dalakvísl summit (Tuffen et al., 2008), which is more erosion-resistant than the  
723 rest of the edifice, and the presence of an actively incising stream to the south and east, where  
724 the lowest elevations occur (**Fig. 3**). If this model is correct, it means that all the samples  
725 collected formed intrusively and have since been exposed by erosion. This perhaps highlights  
726 a characteristic of subglacial rhyolitic edifices, where post quenching hydration serves to

727 further fragment deposits (perlitisation) creating an unconsolidated pile vulnerable to  
728 erosion. By comparison, in fragmental subglacial basaltic deposits, meteoric water causes  
729 cementation and consolidation (palagonisation) of particles to form solid rock (Owen, 2016).

### 730 ***5.8 The relationship between explosive and effusive samples at Dalakvísl***

731         There is a marked difference between water-rich, effusively generated and water-  
732 poor, explosively generated glasses (**Fig. 11**). Mechanisms of magma-water interaction in  
733 basaltic subglacial eruptions are sensitive to pressure, reflected by the marked transition from  
734 pillow lavas to hyaloclastites and hyalotuffs as edifices shoal towards ice surfaces. Explosive  
735 volcanism will be suppressed at depth due to the inhibition of volatile exsolution caused by the  
736 ice/meltwater loading. In basaltic systems this transition typically occurs at depths of ~200 –  
737 500 m, equivalent to ~2 -5 MPa confining pressure (Jones, 1970; Moore and Schilling, 1973;  
738 Allen, 1980; Schopka et al., 2006; Tuffen, 2007; Tuffen, 2010; Owen, 2016). Were eruption  
739 mechanisms at Dalakvísl similarly pressure-controlled? Samples collected from effusive lava  
740 lobes (SPC B) have H<sub>2</sub>O contents consistent with quenching pressures of 2.7-3.7 MPa, whereas  
741 H<sub>2</sub>O contents of the more explosive obsidian sheet samples (SPC A) are consistent with  
742 quenching pressures of 1.8-2.7 MPa (**Fig. 14**). This could indicate a critical pressure threshold  
743 of 2.7 MPa, which determined whether activity was explosive or effusive. However, we think  
744 this unlikely for the following reasons.

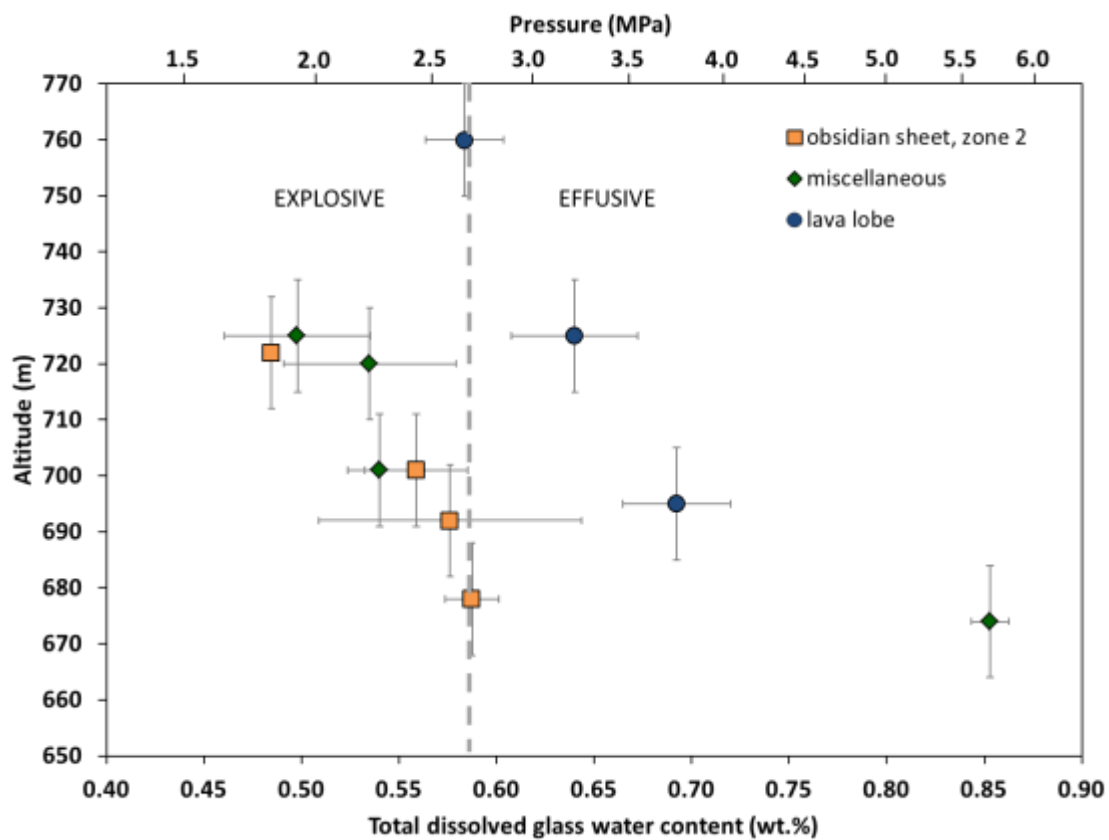
745         Unlike basaltic tuyas, rhyolitic edifices show little vertical variation in the nature of  
746 pyroclasts within the subglacial pile (Tuffen et al., 2002; Smellie, 2007; McGarvie, 2009;  
747 Stevenson et al., 2011; Owen, 2016), suggesting little sensitivity to confining pressure (Tuffen  
748 et al., 2007). Indeed at Dalakvísl, explosive facies would be expected to overlie effusive facies,  
749 however, their spatial distribution (**Fig. 3**) indicates, if anything, lateral rather than vertical

750 divergence in degassing. Furthermore, the lowest elevation obsidian sheet would be expected  
751 to be a similar lithofacies type to the highest elevation lava lobe, due to their similar H<sub>2</sub>O  
752 contents and inferred quenching pressures of 2.7 MPa (Fig. 14). The lithofacies are, however,  
753 very different (compare Figures 2bi-iii to Figures 2ai,ii).

754

755 .

756



757

758 **Figure 14:** Measured magmatic water content-elevation relationships (symbols). Zone 1 sheet samples  
759 are not shown, due to possible non-equilibrium degassing. Pressure estimates use VolatileCalc  
760 (Newman and Lowenstern, 2002), with 0 ppm CO<sub>2</sub> and 800 °C magma temperature. The grey dashed  
761 line indicates the pressure that divides effusive from explosive deposits (2.7 MPa). Error bars as **Figure**  
762 **5.**

763

764 Effusive and explosive deposits predominantly occur in the south and north,  
765 respectively. Therefore it is possible that both styles of activity may have occurred  
766 simultaneously, as inferred for different parts of the Gjálp 1996 fissure eruption  
767 (Guðmundsson et al., 2004). At Gjálp lateral differences in eruption style were mediated by  
768 variations in subglacial cavity pressure, controlled by local meltwater hydrology. Although this  
769 may have occurred at Dalakvísl, vesicularity and degassing of the obsidian sheets is best  
770 explained by a temporal effusive-to-explosive change.

771 Our preferred model is that the transition in style was triggered by a jökulhlaup.  
772 Explosive episodes have been known to follow jökulhlaup induced decompressions during  
773 subglacial basalt eruptions e.g. the 1996 Gjálp eruption (Guðmundsson et al., 2004;  
774 Höskuldsson et al., 2006) and Grímsvötn 2004 (Sigmundsson and Guðmundsson, 2004;  
775 Thordarson and Larsen, 2007; Sigmundsson et al., 2010)). It is unclear whether the  
776 decompression on its own would have been enough to cause a style transition at Dalakvísl. We  
777 suspect that the behavioural change was supplemented by a major change in the degassing  
778 behaviour of the eruption, which was albeit caused by the rapid decompression (Owen et al.,  
779 2013b).

## 780 ***5.9 Is there a link between ice thickness and eruptive style for Torfajökull edifices?***

781 Interestingly, an estimate of 350 m for the Dalakvísl ice thickness is mid-way between  
782 the estimates for the palaeo-ice thickness at Bláhnúkur (400 m (Owen et al., 2012)) and SE  
783 Rauðfossafjöll (290 m (McGarvie et al., 2006; Owen et al., 2013a)). As the eruption style at  
784 Bláhnúkur was effusive (Tuffen et al., 2001; McGarvie, 2009) whereas SE Rauðfossafjöll was  
785 explosive (Tuffen et al., 2002; McGarvie, 2009) and Dalakvísl showed mixed effusive-explosive  
786 behaviour (Tuffen et al., 2008), this could be seen as showing a behavioural response to



787 loading pressure, with edifices that formed under lower pressures being more susceptible to  
788 explosive activity. However, as the inferred ice thicknesses only vary by ~50 m this would  
789 indicate a great behavioural sensitivity towards loading pressure, which seems unlikely as all  
790 of the edifices are  $\geq 140$  m in height and none show a change in lithofacies with elevation  
791 within the subglacial pile. Furthermore, Angel Peak, another subglacial rhyolitic edifice within  
792 Torfajökull, erupted under an inferred ice thickness of just 120 m (Owen et al., 2013a; Owen  
793 and Tuffen, in prep.) and yet erupted effusively. This suggests that ice thickness alone cannot  
794 explain the eruptive behaviour of subglacial rhyolite. Owen et al. (2013a) concluded that there  
795 was no correlation between inferred eruptive style and palaeo-ice thicknesses for subglacial  
796 rhyolitic edifices at Torfajökull. However, the effusively produced edifices (including the  
797 effusive parts of Dalakvísl) had much lower pre-eruptive volatile contents and evidence of  
798 open system degassing, suggesting that the behaviour of subglacial rhyolite is more sensitive  
799 to degassing behaviour than ice thickness.

800

### 801 ***5.10 Conceptual model for the formation of Dalakvísl***

802 We propose that the Dalakvísl eruption began effusively under a relatively high  
803 pressure regime, with loading by juvenile fragmental material up to a relatively flat surface at  
804 810 m a.s.l., overlain by 210 m of ice or ponded meltwater (**Fig. 11**) i.e. with a glacier surface  
805 at ~1,020 m a.s.l. Ponding would favour sustained high meltwater pressure (Guðmundsson et  
806 al., 2004) whilst the lava lobes were being intruded into the pile of poorly consolidated  
807 juvenile hyaloclastite. Quenching pressure variations with elevation led to lava lobe samples  
808 following SPC B in **Figure 11**.

809           Following this, the emplacement of obsidian sheet lithofacies began as the intrusion  
810 of relatively dense bodies of obsidian within a juvenile fragmental deposit. This coincided with  
811 the onset of sudden meltwater drainage; i.e., a jökulhlaup, with a pressure decrease of 1.3  
812 MPa, equivalent to a 130 m drop in hydrostatic head (Owen et al., 2013b). The pressure  
813 reduction allowed sheet margins to degas, but there was insufficient time to adequately  
814 degas dense sheet interiors, which instead responded by forming tiny decompression  
815 bubbles. By the time the obsidian sheets had quenched, the pressure had settled to a level  
816 ~1.3 MPa lower than previous (SPC A in **Fig. 11**). This could be represented by loading from  
817 fragmental material up to 810 m, overlain by ~70 m of ice/meltwater (**Table 5**).

818           Deposits erupted post-jökulhlaup were erupted in a more explosive fashion, with  
819 increased vesicularity and degree of fragmentation. Together with the pressure decrease,  
820 greater explosivity might reflect the shift to a more volatile-rich magma source and closed  
821 system degassing as supported by melt inclusion data from Owen et al. (2013a) and Owen et  
822 al. (2013b) with jökulhlaup-triggered decompression perhaps encouraging the tapping of  
823 more volatile-rich magma from depth. As explosive deposits at Dalakvísl are limited in extent  
824 and small-volume (**Fig. 3**) the explosive phase was likely a brief one.

825           Considerable erosion has occurred at the Dalakvísl edifice in the 70 ka since its  
826 eruption, changing the edifice shape from flat-topped to mound-like and exposing the  
827 sampled outcrops. Erosion is likely to have been driven by both glacial and fluvial processes,  
828 based on the morphology of deep stream-cut valleys on the southern and eastern basal  
829 margins (**Fig. 3**) and the local presence of younger basaltic hyaloclastite deposits, associated  
830 with reworked glacial tills, overlying the eroded upper surface of Dalakvísl formation rhyolites  
831 (Tuffen et al. 2008).

## 832        **6 Conclusion**

833        We have used the dissolved volatile content of rhyolitic glasses erupted in mixed effusive-  
834 explosive activity at Dalakvísl, Torfajökull, Iceland to infer quenching pressures and thus to  
835 place constraints on plausible syn-eruptive ice thicknesses. When grouped by lithofacies,  
836 there are decreasing trends of H<sub>2</sub>O content with elevation, consistent with degassing in a  
837 subglacial environment. However, there is H<sub>2</sub>O variation, both between lithofacies types and  
838 between different vesicularity zones within obsidian sheets; the dense cores (zone 1) are  
839 more water-rich than the more vesicular outer portion (zone 2) of the sheets.

840        Solubility pressure curves (SPCs) are used to model H<sub>2</sub>O variations with elevation, and  
841 to reconstruct loading by ice, meltwater and volcanic deposits. Best model fits to data indicate  
842 loading by fragmental deposits and ice/water, implying that all sampled outcrops formed  
843 intrusively and have experienced significant erosion. They also suggest that the original  
844 edifice morphology was flat-topped, with a similar summit elevation to today (810 m), and  
845 therefore greatest erosion is from the edifice margins, consistent with present-day stream  
846 incision. Samples from obsidian sheet cores do not follow any SPC and are proposed to have  
847 degassed in disequilibrium, due to large diffusion distances in vesicle-poor magma and  
848 relatively rapid decompression.

849        Most of the data can be plotted to two SPCs, suggesting that two distinct pressure  
850 regimes operated during the eruption – a higher-pressure regime accompanied by effusive  
851 eruption style and a lower-pressure regime dominated by explosive activity. Various scenarios  
852 were modelled, including pressure changes due to variation in ice loading, tephra  
853 accumulation, subglacial cavity pressure, and water level. Our preferred model is for abrupt  
854 drainage of ponded meltwater in a jökulhlaup, to trigger rapid depressurisation to a lower

855 pressure regime (pressure drop of 1.3 MPa, equivalent to 130 m hydrostatic head) and more  
856 explosive activity.

857 Best-fit models to the water-rich, early-formed lava lobes suggest up to 210 m of ice  
858 loading, with an ice surface at 930–1,020 m a.s.l., depending on the proportion of overlying  
859 fragmental material to water/ice. The upper limit fits well with independent estimates of ice  
860 surface elevation from nearby, contemporaneous tuyas, implying an initial glacier thickness  
861 of ~350 m. Interestingly, the thickness of the ice seems to have had little influence on eruptive  
862 behaviour, although it is possible that a rapid pressure change triggered the transition in style.

863 This paper highlights how dissolved volatile contents can provide useful insights into  
864 syn-eruptive ice thickness, edifice loading and subglacial drainage during rhyolitic eruptions  
865 under ice, provided that a large and representative sample suite is acquired, and there is a  
866 good understanding of lithofacies formation.

## 867 **7 Acknowledgements**

868 We thank the Icelandic Environment Agency, the Icelandic Centre for Research and  
869 the Icelandic Institute of Natural History for permission to conduct fieldwork and collect  
870 samples in the Fjallabak Nature Reserve. JO was funded by NERC studentship NE/G523439/1,  
871 whereas HT acknowledges NERC grants NE/G000654/1, NE/E013740/1 and a Royal Society  
872 University Research Fellowship. DMcG was supported by the Open University staff Tutor  
873 Research and Scholarship Fund. Thanks to Ferðafélag Íslands, particularly the team at  
874 Landmannalaugar (Helga, Benedikta, Rakel, Bjarney) and Fjallafang (Nína, Smári, Orri, Sarah),  
875 plus C Valentine, A Wilkinson, W Gosling, S Flude, N Odling and C Petrone for laboratory  
876 assistance, H Pinkerton, L Wilson, P Wynn, J Gilbert, M James and J Stevenson for productive  
877 discussions and J Dixon, B Edwards, S Lane and M Humphreys and others for useful edits. HT

878 thanks the Lancaster University Facilities and Sports Centre teams for life-saving first aid and  
879 JO is grateful to the NHS and care of N Kalenderoglou. Final thanks go to J Lowenstern and M  
880 Hartley for thorough and insightful reviews which greatly improved the manuscript and  
881 especially to GB Kristjánsdóttir for an incredibly keen editorial eye.

## 882 **8 References**

- 883 Allen, C.C., 1980. Icelandic Subglacial Volcanism: Thermal and Physical Studies. *J Geol*,  
884 88(1): 108-117. 10.1086/628478
- 885 Blake, S., 1984. Magma mixing and hybridization processes at the alkalic, silicic, Torfajökull  
886 central volcano triggered by tholeiitic Veidivötn fissuring, south Iceland. *J Volcanol*  
887 *Geoth Res*, 22(1-2): 1-31. 10.1016/0377-0273(84)90033-7
- 888 Brendryen, J., Haflidason, H. and Sejrup, H.P., 2010. Norwegian Sea tephrostratigraphy of  
889 marine isotope stages 4 and 5: Prospects and problems for tephrochronology in the  
890 North Atlantic region. *Quaternary Sci Rev*, 29(7-8): 847-864.  
891 10.1016/j.quascirev.2009.12.004
- 892 Castro, J.M. and Gardner, J.E., 2008. Did magma ascent rate control the explosive-effusive  
893 transition at the Inyo volcanic chain, California? *Geology*, 36(4): 279-282.  
894 10.1130/g24453a.1
- 895 Denton, J.S., Tuffen, H., Gilbert, J.S. and Odling, N., 2009. The hydration and alteration of  
896 perlite and rhyolite. *J Geol Soc London*, 166: 895-904. 10.1144/0016-76492008-007
- 897 Di Muro, A., Villemant, B., Montagnac, G., Scaillet, B. and Reynard, B., 2006. Quantification  
898 of water content and speciation in natural silicic glasses (phonolite, dacite, rhyolite) by  
899 confocal microRaman spectrometry. *Geochim Cosmochim Acta*, 70(11): 2868-2884.  
900 DOI 10.1016/j.gca.2006.02.016
- 901 Dixon, J.E., 1997. Degassing of alkalic basalts. *Am Mineral*, 82: 368-378.  
902 <https://doi.org/10.2138/am-1997-3-415>
- 903 Dixon, J.E. and Clague, D.A., 2001. Volatiles in basaltic glasses from Loihi Seamount, Hawaii:  
904 Evidence for a relatively dry plume component. *J Petrol*, 42(3): 627-654.  
905 <https://doi.org/10.1093/petrology/42.3.627>
- 906 Dixon, J.E., Filiberto, J.R., Moore, J.G. and Hickson, C.J., 2002. Volatiles in basaltic glasses  
907 from a subglacial volcano in northern British Columbia (Canada): implications for ice  
908 sheet thickness and mantle volatiles. In: J.L. Smellie and M.G. Chapman (Editors),  
909 Volcano-Ice interaction on Earth and Mars. Geological Society Special Publication No.  
910 202, 255-271. 10.1144/gsl.sp.2002.202.01.13
- 911 Dixon, J.E. and Stolper, E.M., 1995. An Experimental Study of Water and Carbon Dioxide  
912 Solubilities in Mid-Ocean Ridge Basaltic Liquids. Part II: Applications to Degassing. *J*  
913 *Petrol*, 36(6): 1633-1646. <https://doi.org/10.1093/oxfordjournals.petrology.a037268>
- 914 Dixon, J.E., Stolper, E.M. and Holloway, J.R., 1995. An Experimental Study of Water and  
915 Carbon Dioxide Solubilities in Mid-Ocean Ridge Basaltic Liquids. Part I: Calibration  
916 and Solubility Models. *J Petrol*, 36(6): 1607-1631.  
917 <https://doi.org/10.1093/oxfordjournals.petrology.a037267>

918 Duncan, A.M., Chester, D.K. and Guest, J.E., 1986. Volcanism in Italy: The Hazard  
919 Implications of Hydromagmatic Eruptions. *Interdiscipl Sci Rev*, 11(4): 377-385.  
920 10.1179/isr.1986.11.4.377

921 Edwards, B.R., Russell, J. and Simpson, K., 2011. Volcanology and petrology of Mathews  
922 Tuya, northern British Columbia, Canada: glaciovolcanic constraints on interpretations  
923 of the 0.730 Ma Cordilleran paleoclimate. *B Volcanol*, 73(5): 479-496.  
924 10.1007/s00445-010-0418-z

925 Edwards, B.R., Skilling, I.P., Cameron, B., Haynes, C., Lloyd, A. and Hungerford, J.H.D.,  
926 2009. Evolution of an englacial volcanic ridge: Pillow Ridge tinda, Mount Edziza  
927 volcanic complex, NCVP, British Columbia, Canada. *J Volcanol Geoth Res*, 185(4):  
928 251-275. 10.1016/j.jvolgeores.2008.11.015

929 Frost, B.R. and Frost, C.D., 2008. A Geochemical Classification for Feldspathic Igneous  
930 Rocks. *J Petrol*, 49(11): 1955-1969. 10.1093/petrology/egn054

931 Furnes, H., Fridleifsson, I.B. and Atkins, F.B., 1980. Subglacial volcanics - on the formation  
932 of acid hyaloclastites. *J Volcanol Geoth Res*, 8(1): 95-110.  
933 [https://doi.org/10.1016/0377-0273\(80\)90009-8](https://doi.org/10.1016/0377-0273(80)90009-8)

934 Gardner, J.E., Hilton, M. and Carroll, M.R., 1999. Experimental constraints on degassing of  
935 magma: isothermal bubble growth during continuous decompression from high  
936 pressure. *Earth Planet Sc Lett*, 168: 201-218. [https://doi.org/10.1016/S0012-](https://doi.org/10.1016/S0012-821X(99)00051-5)  
937 [821X\(99\)00051-5](https://doi.org/10.1016/S0012-821X(99)00051-5)

938 Gonnermann, H.M. and Manga, M., 2007. The fluid mechanics inside a volcano. *Annu Rev*  
939 *Fluid Mech*, 39: 321-356. <https://doi.org/10.1146/annurev.fluid.39.050905.110207>

940 Guðmundsson, M.T., 2003. Melting of ice by magma-ice-water interactions during subglacial  
941 eruptions as an indicator of heat transfer in subaqueous eruptions. In: J.D.L. White, J.L.  
942 Smellie and D. Clague (Editors), *Explosive subaqueous volcanism*. American  
943 Geophysical Union Monograph, pp. 61-72.

944 Guðmundsson, M.T., 2005. 6. Subglacial volcanic activity in Iceland. In: C. Caseldine, A.  
945 Russell, J. Harðardóttir and Ó. Knudsen (Editors), *Developments in Quaternary*  
946 *Sciences*. Elsevier, New York, pp. 127-151. 10.1016/s1571-0866(05)80008-9

947 Guðmundsson, M.T., Sigmundsson, F., Björnsson, H. and Högnadóttir, T., 2004. The 1996  
948 eruption at Gjalp, Vatnajökull ice cap, Iceland: efficiency of heat transfer, ice  
949 deformation and subglacial water pressure. *B Volcanol*, 66(1): 46-65. 10.1007/s00445-  
950 003-0295-9

951 Gunnarsson, B., Marsh, B.D. and Taylor Jr, H.P., 1998. Generation of Icelandic rhyolites:  
952 silicic lavas from the Torfajökull central volcano. *J Volcanol Geoth Res*, 83(1-2): 1-45.  
953 10.1016/s0377-0273(98)00017-1

954 Hooke, R.L., 1984. On the role of mechanical energy in maintaining subglacial water conduits  
955 at atmospheric pressure. *J Glaciol*, 30(105): 180-187. 10.3189/s0022143000005918

956 Höskuldsson, Á. and Sparks, R.S.J., 1997. Thermodynamics and fluid dynamics of effusive  
957 subglacial eruptions. 59(3): 219-230. 10.1007/s004450050187

958 Höskuldsson, Á., Sparks, R.S.J. and Carroll, M.R., 2006. Constraints on the dynamics of  
959 subglacial basalt eruptions from geological and geochemical observations at Kverkfjöll,  
960 NE-Iceland. *B Volcanol*, 68(7-8): 689-701. 10.1007/s00445-005-0043-4

961 Ihinger, P.D., Zhang, Y.X. and Stolper, E.M., 1999. The speciation of dissolved water in  
962 rhyolitic melt. *Geochim Cosmochim Ac*, 63(21): 3567-3578.  
963 [https://doi.org/10.1016/S0016-7037\(99\)00277-X](https://doi.org/10.1016/S0016-7037(99)00277-X)

964 Imsland, P., 1983. Iceland and the ocean floor. Comparison of chemical characteristics of the  
965 magmatic rocks and some volcanic features. *Contrib Mineral Petr*, 83(1): 31-37.  
966 10.1007/bf00373076

- 967 Jones, J.G., 1966. Intraglacial volcanoes of South-West Iceland and their significance in the  
968 interpretation of the form of the marine basaltic volcanoes. *Nature*, 212(5062): 586-  
969 588. 10.1038/212586a0
- 970 Jones, J.G., 1970. Intraglacial Volcanoes of the Laugarvatn Region, Southwest Iceland, II. *J*  
971 *Geol*, 78(2): 127-140. <https://doi.org/10.1086/627496>
- 972 Larsen, G., 1984. Recent volcanic history of the Veidivötn fissure swarm, southern Iceland --  
973 an approach to volcanic risk assessment. *J Volcanol Geoth Res*, 22(1-2): 33-58.  
974 10.1016/0377-0273(84)90034-9
- 975 Larsen, J.F. and Gardner, J.E., 2000. Experimental constraints on bubble interactions in  
976 rhyolite melts: implications for vesicle size distributions. *Earth Planet Sc Lett*, 180(1-  
977 2): 201-214. 10.1016/S0012-821X(00)00166-7
- 978 Leschik, M., Heide, G., Frischat, G.H., Behrens, H., Wiedenbeck, M., Wagner, N., Heide, K.,  
979 Geißler, H. and Reinholz, U., 2004. Determination of H<sub>2</sub>O and D<sub>2</sub>O contents in rhyolitic  
980 glasses. *Phys Chem Glasses*, 45(4): 238-251.
- 981 MacDonald, R., McGarvie, D.W., Pinkerton, H., Smith, R.L. and Palavz, A., 1990.  
982 Petrogenetic evolution of the Torfajökull Volcanic Complex, Iceland I. Relationship  
983 between the magma types. *J Petrol*, 31(2): 429-459. 10.1093/petrology/31.2.429
- 984 Macpherson, G.J., 1984. A model for predicting the volumes of vesicles in submarine basalts.  
985 *J Geol*, 92(1): 73-82. [www.jstor.org/stable/30062132](http://www.jstor.org/stable/30062132)
- 986 Mangan, M. and Sisson, T., 2000. Delayed, disequilibrium degassing in rhyolite magma:  
987 decompression experiments and implications for explosive volcanism. *Earth Planet Sc*  
988 *Lett*, 183(3-4): 441-455. [http://dx.doi.org/10.1016/S0012-821X\(00\)00299-5](http://dx.doi.org/10.1016/S0012-821X(00)00299-5)
- 989 Martin, E. and Sigmarsson, O., 2007. Crustal thermal state and origin of silicic magma in  
990 Iceland: the case of Torfajökull, Ljósufjöll and Snæfellsjökull volcanoes. *Contrib*  
991 *Mineral Petr*, 153(5): 593-605. 10.1007/s00410-006-0165-5
- 992 Martin, E. and Sigmarsson, O., 2010. Thirteen million years of silicic magma production in  
993 Iceland: Links between petrogenesis and tectonic settings. *Lithos*, 116(1-2): 129-144.  
994 10.1016/j.lithos.2010.01.005
- 995 Mastin, L.G., Christiansen, R.L., Thornber, C., Lowenstern, J. and Beeson, M., 2004. What  
996 makes hydromagmatic eruptions violent? Some insights from the Keanakāko'i Ash,  
997 Kīlauea Volcano, Hawai'i. *J Volcanol Geoth Res*, 137(1-3): 15-31.  
998 10.1016/j.jvolgeores.2004.05.015
- 999 Mathews, W.H., 1947. Tuya, Flat-Topped Volcanoes in Northern British-Columbia. *Am J*  
1000 *Sci*, 245(9): 560-570. 10.2475/ajs.245.9.560
- 1001 McGarvie, D.W., 1984. Torfajökull: A volcano dominated by magma mixing. *Geology*,  
1002 12(11): 685-688. 10.1130/0091-7613(1984)12<685:tavdbm>2.0.co;2
- 1003 McGarvie, D.W., 2009. Rhyolitic volcano-ice interactions in Iceland. *J Volcanol Geoth Res*,  
1004 185(4): 367-389. 10.1016/j.jvolgeores.2008.11.019
- 1005 McGarvie, D.W., Burgess, R., Tindle, A.G., Tuffen, H. and Stevenson, J.A., 2006. Pleistocene  
1006 rhyolitic volcanism at Torfajökull, Iceland: eruption ages, glaciovolcanism, and  
1007 geochemical evolution. *Jökull*, 56: 57-75.
- 1008 McGarvie, D.W., MacDonald, R., Pinkerton, H. and Smith, R.L., 1990. Petrogenetic Evolution  
1009 of the Torfajökull Volcanic Complex, Iceland II. The Role of Magma Mixing. *J Petrol*,  
1010 31(2): 461-481. 10.1093/petrology/31.2.461
- 1011 McGarvie, D.W., Stevenson, J.A., Burgess, R., Tuffen, H. and Tindle, A.G., 2007. Volcano-  
1012 ice interactions at Prestahnúkur, Iceland: rhyolite eruption during the last interglacial-  
1013 glacial transition. *Ann Glaciol*, 45(1): 38-47.  
1014 <https://doi.org/10.3189/172756407782282453>
- 1015 Moore, J.G., 1965. Petrology of deep sea basalt near Hawaii. *Am J Sci*, 263(1): 40-52.  
1016 10.2475/ajs.263.1.40

1017 Moore, J.G. and Schilling, J.-G., 1973. Vesicles, water, and sulfur in Reykjanes Ridge basalts.  
1018 Contrib Mineral Petr, 41(2): 105-118. 10.1007/bf00375036

1019 Newman, S., Epstein, S. and Stolper, E., 1988. Water, carbon dioxide, and hydrogen isotopes  
1020 in glasses from the ca. 1340 A.D. eruption of the Mono Craters, California: Constraints  
1021 on degassing phenomena and initial volatile content. J Volcanol Geoth Res, 35(1–2):  
1022 75-96. 10.1016/0377-0273(88)90007-8

1023 Newman, S. and Lowenstern, J.B., 2002. VolatileCalc: a silicate melt–H<sub>2</sub>O–CO<sub>2</sub> solution  
1024 model written in Visual Basic for excel. Comput Geosci, 28(5): 597-604.  
1025 10.1016/s0098-3004(01)00081-4

1026 Newman, S., Stolper, E.M. and Epstein, S., 1986. Measurement of water in rhyolitic glasses:  
1027 calibration of an infrared spectroscopic technique. 71(11-12): 1527-1541.

1028 Nichols, A.R.L., Carroll, M.R. and Höskuldsson, Á., 2002. Is the Iceland hot spot also wet?  
1029 Evidence from the water contents of undegassed submarine and subglacial pillow  
1030 basalts. Earth Planet Sc Lett, 202(1): 77-87. 10.1016/S0012-821X(02)00758-6.

1031 Nichols, A.R.L. and Wysoczanski, R.J., 2007. Using micro-FTIR spectroscopy to measure  
1032 volatile contents in small and unexposed inclusions hosted in olivine crystals. Chem  
1033 Geol, 242(3–4): 371-384. 10.1016/j.chemgeo.2007.04.007

1034 Okumura, S., Nakamura, M. and Nakashima, S., 2003. Determination of molar absorptivity of  
1035 IR fundamental OH-stretching vibration in rhyolitic glasses. Am Mineral, 88(11-12):  
1036 1657-1662. <https://doi.org/10.2138/am-2003-11-1204>

1037 Owen, J., 2013. Volatiles in Icelandic subglacial rhyolite. PhD thesis, Lancaster University.

1038 Owen, J., 2016. Using volatiles in magma to decipher subglacial eruption dynamics. Geology  
1039 Today, 32(1): 30-37. 10.1111/gto.12127

1040 Owen, J. and Tuffen, H., in prep. On what type of volcanic edifice can you use the magma  
1041 degassing technique for reconstructing palaeo-ice thicknesses?

1042 Owen, J., Tuffen, H. and McGarvie, D.W., 2012. Using dissolved H<sub>2</sub>O in rhyolitic glasses to  
1043 estimate palaeo-ice thickness during a subglacial eruption at Bláhnúkur (Torfajökull,  
1044 Iceland). B Volcanol, 74(6): 1355-1378. 10.1007/s00445-012-0601-5

1045 Owen, J., Tuffen, H. and McGarvie, D.W., 2013a. Explosive subglacial rhyolitic eruptions in  
1046 Iceland are fuelled by high magmatic H<sub>2</sub>O and closed system degassing. Geology,  
1047 41(2): 251-254. **10.1130/G33647.1**

1048 Owen, J., Tuffen, H. and McGarvie, D.W., 2013b. Pre-eruptive volatile content, degassing  
1049 paths and depressurisation explaining the transition in style at the subglacial rhyolitic  
1050 eruption of Dalakvísl, South Iceland. J Volcanol Geoth Res, 258: 143–162.  
1051 <https://doi.org/10.1016/j.jvolgeores.2013.03.021>

1052 Proussevitch, A.A. and Sahagian, D.L., 1996. Dynamics of coupled diffusive and  
1053 decompressive bubble growth in magmatic systems. J Geophys Res, 101(B8): 17447-  
1054 17455. <https://doi.org/10.1029/96JB01342>

1055 Rutherford, M.J., 2008. Magma Ascent Rates. In: K.D. Putirka and F.J. Tepley III (Editors),  
1056 Minerals, Inclusions and Volcanic Processes. Reviews in Mineralogy and  
1057 Geochemistry, 69, 241-271. DOI 10.2138/rmg.2008.69.7

1058 Sæmundsson, K., 1972. Jarðfræðiglefsur um Torfajökulssvæðið. Naturufræðingurinn, 42: 81–  
1059 99.

1060 Sæmundsson, K., 1979. Outline of the geology of Iceland. Jökull, 29: 7-28.

1061 Saubin, E., Tuffen, H., Gurioli, L., Owen, J., Castro, J.M., Berlo, K., McGowan, E., Schipper,  
1062 C.I. and Wehbe, K., 2016. Conduit dynamics in transitional rhyolitic activity recorded  
1063 by tuffisite vein textures from the 2008-2009 Chaitén eruption. Front Earth Sci, 4.  
1064 10.3389/feart.2016.00059

1065 Schopka, H.H., Guðmundsson, M.T. and Tuffen, H., 2006. The formation of Helgafell,  
1066 southwest Iceland, a monogenetic subglacial hyaloclastite ridge: Sedimentology,



1067 hydrology and volcano-ice interaction. *J Volcanol Geoth Res*, 152(3-4): 359-377.  
1068 10.1016/j.jvolgeores.2005.11.010

1069 Sigmundsson, F. and Guðmundsson, M.T., 2004. Gos í Grímsvötnum 1. – 6. nóvember 2004.  
1070 Jökull, 54: 139-142.

1071 Sigmundsson, F., Pinel, V., Lund, B., Albino, F., Pagli, C., Geirsson, H. and Sturkell, E., 2010.  
1072 Climate effects on volcanism: influence on magmatic systems of loading and unloading  
1073 from ice mass variations, with examples from Iceland. *Philos T R Soc A*, 368(1919):  
1074 2519-2534. 10.1098/rsta.2010.0042

1075 Sigurdsson, H., 1977. Generation of Icelandic rhyolites by melting of plagiogranites in the  
1076 oceanic layer. *Nature*, 269(5623): 25-28. 10.1038/269025a0

1077 Smellie, J.L., 2007. Quaternary volcanism: subglacial landforms. In: S.A. Elias (Editor),  
1078 *Encyclopedia of Quaternary Sciences*. Elsevier, Amsterdam.

1079 Sparks, R.S.J. and Brazier, S., 1982. New Evidence for Degassing Processes during Explosive  
1080 Eruptions. *Nature*, 295(5846): 218-220. 10.1038/295218a0

1081 Stevenson, J.A., 2011. Grímsvötn 2 – What was in the plume?, Volcan01010.

1082 Stevenson, J.A., Gilbert, J.S., McGarvie, D.W. and Smellie, J.L., 2011. Explosive rhyolite tuya  
1083 formation: classic examples from Kerlingarfjöll, Iceland. *Quaternary Sci Rev*, 30(1-2):  
1084 192-209. 10.1016/j.quascirev.2010.10.011

1085 Stevenson, J.A., Smellie, J.L., McGarvie, D.W., Gilbert, J.S. and Cameron, B.I., 2009.  
1086 Subglacial intermediate volcanism at Kerlingarfjöll, Iceland: Magma-water interactions  
1087 beneath thick ice. *J Volcanol Geoth Res*, 185(4): 337-351.  
1088 10.1016/j.jvolgeores.2008.12.016

1089 Stolper, E., 1982. Water in silicate-glasses: An infrared spectroscopic study. *Contrib Mineral*  
1090 *Petr*, 81(1): 1-17. <https://doi.org/10.1007/BF00371154>

1091 Thordarson, T. and Larsen, G., 2007. Volcanism in Iceland in historical time: Volcano types,  
1092 eruption styles and eruptive history. *J Geodyn*, 43(1): 118-152.  
1093 10.1016/j.jog.2006.09.005

1094 Tómasson, H., 1996. The jökulhlaup from Katla in 1918. *Ann Glaciol*, 22: 249-254.  
1095 10.1017/S0260305500015494

1096 Tuffen, H., 2007. Models of ice melting and edifice growth at the onset of subglacial basaltic  
1097 eruptions. *J Geophys Res*, 112(B3). 10.1029/2006JB004523

1098 Tuffen, H., 2010. How will melting of ice affect volcanic hazards in the twenty-first century?  
1099 *Philos T R Soc A*, 368(1919): 2535-2558. 10.1098/rsta.2010.0063

1100 Tuffen, H. and Castro, J.M., 2009. The emplacement of an obsidian dyke through thin ice:  
1101 Hrafninnuhryggur, Krafla Iceland. *J Volcanol Geoth Res*, 185(4): 352-366.  
1102 10.1016/j.jvolgeores.2008.10.021

1103 Tuffen, H., Gilbert, J. and McGarvie, D., 2001. Products of an effusive subglacial rhyolite  
1104 eruption: Bláhnúkur, Torfajökull, Iceland. *B Volcanol*, 63(2): 179-190.  
1105 10.1007/s004450100134

1106 Tuffen, H., McGarvie, D.W. and Gilbert, J.S., 2007. Will subglacial rhyolite eruptions be  
1107 explosive or intrusive? Some insights from analytical models. *Ann Glaciol*, 45(1): 87-  
1108 94. 10.3189/172756407782282534

1109 Tuffen, H., McGarvie, D.W., Gilbert, J.S. and Pinkerton, H., 2002. Physical volcanology of a  
1110 subglacial-to-emergent rhyolitic tuya at Rauðufossafjöll, Torfajökull, Iceland. In: J.L.  
1111 Smellie and M.G. Chapman (Editors), *Volcano-Ice interaction on Earth and Mars*.  
1112 *Geological Society Special Publication No. 202*, 213-236.  
1113 <https://doi.org/10.1144/GSL.SP.2002.202.01.11>

1114 Tuffen, H., McGarvie, D.W., Pinkerton, H., Gilbert, J.S. and Brooker, R.A., 2008. An  
1115 explosive-intrusive subglacial rhyolite eruption at Dalakvísl, Torfajökull, Iceland. *B*  
1116 *Volcanol*, 70(7): 841-860. 10.1007/s00445-007-0174-x

- 1117 Tuffen, H., Owen, J. and Denton, J., 2010. Magma degassing during subglacial eruptions and  
1118 its use to reconstruct palaeo-ice thicknesses. *Earth-Sci Rev*, 99(1-2): 1-18.  
1119 10.1016/j.earscirev.2010.01.001
- 1120 Xu, Z. and Zhang, Y., 2002. Quench rates in air, water, and liquid nitrogen, and inference of  
1121 temperature in volcanic eruption columns. *Earth Planet Sc Lett*, 200(3-4): 315-330.  
1122 10.1016/s0012-821x(02)00656-8
- 1123 Yokoyama, T., Okumura, S. and Nakashima, S., 2008. Hydration of rhyolitic glass during  
1124 weathering as characterized by IR microspectroscopy. *Geochim Cosmochim Ac*, 72(1):  
1125 117-125. 10.1016/j.gca.2007.10.018
- 1126 Zellmer, G.F., Rubin, K.H., Grönvold, K. and Jurado-Chichay, Z., 2008. On the recent bimodal  
1127 magmatic processes and their rates in the Torfajökull–Veidivötn area, Iceland. *Earth*  
1128 *Planet Sc Lett*, 269(3-4): 388-398. 10.1016/j.epsl.2008.02.026  
1129